

# A thermodynamically-motivated model for stress-fiber reorganization

A. Vigliotti<sup>¶‡</sup>, W. Ronan<sup>¶</sup>, F.P.T. Baaijens<sup>§</sup> and V.S. Deshpande<sup>¶<sup>1</sup></sup>

<sup>¶</sup>Department of Engineering, University of Cambridge, Cambridge CB2 1PZ, U.K.

<sup>§</sup>Department of Biomedical Engineering, Eindhoven University of Technology, PO Box 513, 5600 Eindhoven, MB, The Netherlands.

<sup>‡</sup>Innovative Materials Laboratory, Italian Aerospace Research Centre, Capua 81043, Italy

## Abstract

We present a model for stress-fiber reorganization and the associated contractility that includes both the kinetics of stress-fiber formation and dissociation as well as the kinetics of stress-fiber remodeling. These kinetics are motivated by considering the enthalpies of the actin/myosin functional units that constitute the stress-fibers. The stress, strain and strain-rate dependence of the stress-fiber dynamics are natural outcomes of the approach. The model is presented in a general three-dimensional framework and includes the transport of the unbound stress-fiber proteins. Predictions of the model for a range of cyclic loadings are illustrated to rationalize hitherto apparently contrasting observations. These observations include: (i) For strain amplitudes around 10% and cyclic frequencies of about 1 Hz, stress-fibers align perpendicular to the straining direction in cells subjected to cyclic straining on a 2D substrate while the stress-fibers align parallel with the straining direction in cells constrained in a 3D tissue. (ii) At lower applied cyclic frequencies, stress-fibers in cells on 2D substrates display no sensitivity to symmetric applied strain versus time waveforms but realign in response to applied loadings with a fast lengthening rate and slow shortening. (iii) At very low applied cyclic frequencies (on the order of mHz) with symmetric strain versus time waveforms, cells on 2D substrates orient perpendicular to the direction of cyclic straining above a critical strain amplitude.

**Keywords:** *mechano-sensitivity; actin/myosin contractility; stress-fibers; cytoskeleton.*

---

<sup>1</sup> Author for correspondence (vsd@eng.cam.ac.uk)

## 1. Introduction

The cytoskeletal arrangement within cells is sensitive to their mechanical and chemical environments as well as the imposed loadings. For example, on stiff continuous substrates (Discher et al. 2005) or on substrates comprising an array of stiff micro-posts (Tan et al. 2003) cells form a strong network of actin/myosin stress-fibers while the same cells when placed on more compliant continuous or micro-post substrates form weak cytoskeletal networks. Similarly, cells seeded on substrates with ligand patterns develop specific actin and focal adhesion distributions that are a function of the ligand patterns shape and size (Parker et al. 2002; Chen et al. 2003). In turn, the cell's cytoskeleton influences a broad range of cellular activities. For example, cytoskeletal arrangements in arterial endothelial cells affect intracellular signaling and gene expression which regulate cellular functions such as apoptosis, proliferation and morphology (Wang and Thampatty 2006).

Experiments regarding cytoskeletal arrangements in response to cyclic mechanical stimuli were initially performed on cells seeded on two-dimensional substrates that were stiff relative to the cells (Neidlinger-Wilke et al. 2001; Kaunas et al. 2005). In these experiments the cytoskeletal network formed perpendicular to the imposed cyclic strains and this was interpreted as strain avoidance (Buck 1980). Typically this avoidance increased with increasing imposed strain amplitude at a fixed frequency of loading (Kaunas et al. 2005). This was interpreted as a sensitivity to imposed strain-rate (Wei et al. 2008). This hypothesis was further reinforced by the experiments of Tondon et al. (2012) who demonstrated reduced sensitivity of cells subjected to fixed strain amplitudes but reduced frequencies of applied loading. However, this explanation contrasts with the observations of Faust et al. (2011) who performed experiments with a fixed (low) value of applied strain-rate and varied the strain amplitude. The cells they investigated showed an increased strain avoidance when the imposed strain amplitude was increased beyond a critical value suggesting a sensitivity to strain amplitude rather than strain-rate. All the observations mentioned above typically involved triangular (or near triangular) imposed strain versus time waveforms. Tondon et al. (2012) reported a strong sensitivity of the observed cytoskeletal arrangements to the shape of imposed strain waveform using asymmetrical triangular and square strain versus time waveforms. Using these observations, Tondon et al (2012) concluded that the cytoskeletal arrangements are more sensitive to the lengthening rate compared to the shortening rate.

More recently, cells have also been cultured in a three-dimensional (3D) matrix or gel. In a static setting the contractile stresses exerted by the cells lead to compaction of the unconstrained construct in all directions (Foolen et al. 2012). If the construct is uniaxially constrained, the cytoskeleton of the cells orients in the constrained direction (Neiponice et al. 2007) but surprisingly this preference remains even when cyclic strains are applied (Gauvin et al. 2011; Nieponice et al. 2007), i.e. in a 3D setting cyclic loading the cytoskeleton seems to align with the imposed strain direction while in 2D settings the cells exhibit strain avoidance.

Phenomenological cytoskeleton remodeling models have been proposed to rationalize such contrasting phenomena. These models include the stress, strain and strain-rate dependence of the stress-fiber kinetics using phenomenological relations. However, these models are typically unable to account for the full range of observations. For example, the models of Deshpande et al. (2006) and Vernerey and Farsad (2011) accurately predict the strain avoidance for the cyclic response of cells on 2D substrates but cannot model the alignment of the stress-fibers with the imposed strain in 3D. On the other hand, the model proposed by Obbink-Huizer et al. (2014) is able to account for the cyclic response of cells in both the 2D

and 3D settings by including a strain dependence in the stress-fiber kinetics. However, this model has the critical shortcoming that strain dependence is difficult to justify over an extended time period when the cells are expected to remodel and lose strain memory. Moreover, none of the approaches presented to-date can rationalize all the observations mentioned above together, and especially the dependence on the shape of the imposed strain versus time waveforms.

### *1.1 Review of the key biochemical processes and experimental observations*

In the suspended or resting state, short actin filaments in the cytoplasm are surrounded by a pool of actin monomers bound to profilin. Myosin II exists in the bent state in which the tail domain interacts with the motor head. The formation of stress-fibers in the cell is triggered by an activation signal in the form of either a nervous impulse, an external signal or signaling from focal adhesions. Several parallel intracellular pathways are involved. For example, adhesion to the extracellular matrix triggers a signaling pathway from focal adhesions through Rho GTPase and ROCK (Rho-associated protein kinase) with phosphorylation of NMM2 (non-muscle myosin II). This involves (i) the activation of Rho due to the clustering of high affinity integrins, (ii) the simultaneous diffusion and de-phosphorylation of Rho molecules through the cell, (iii) the activation of ROCK by the Rho and finally (iv) the formation of stress-fibers comprising actin and NMM2: these fibers generate tension by cross-bridge cycling between the actin and the myosin filaments.

These bio-chemical processes are associated with the following key experimental observations of stress-fiber development in cells:

- (i) Substantial evidence supports the idea that tension contributes to the formation of stress-fibers. For example, free-floating gels contract over several days, by as much 90%, even though they lack stress-fibers (Burridge and Chrzanowska-Wodnicka 1996). If the gels are anchored, isometric tension is generated and the fibroblasts develop prominent stress-fibers (Mochitate et al. 1991). Upon release of the tension, the attached gels rapidly contract. Moreover, when force is applied locally, an actin filament bundle is induced immediately adjacent to its application site (Kolega 1986). Associated with the tension-dependent stress-fiber assembly is the development of structural anisotropy. For example, uniaxially constrained, fibroblast-populated collagen gels develop a high degree of fiber alignment and mechanical anisotropy, while gels constrained biaxially remain isotropic (Thomopoulos et al. 2005).
- (ii) Cells “sense” the stiffness of their substrates and exert smaller tractions on more compliant substrates (Discher et al. 2005).
- (iii) When substrates on which cells are cultured are subjected to cyclic strains, cells “avoid strain” such that stress-fibers form in the direction perpendicular to the imposed cyclic strain (Kaunas et al. 2005). On the other hand, when cells cultured in three-dimensional (3D) tissues are subjected to cyclic strain, “strain alignment” is observed such that stress-fibers now form in the direction of the imposed cyclic strain (Nieponice et al. 2007).
- (iv) A strong stress-fiber network forms in cells subjected to uniaxial stress states but biaxially constrained cells form weaker stress-fiber networks (Thavandiran et al. 2013).

In this study we develop a micro-mechanical approach for the constitutive law for stress-fiber contractility within cells. The model will employ thermodynamic considerations to motivate the dependence of stress-fiber kinetics on stress, strain and strain-rate.

## 2. Formulation of a thermodynamically-motivated model

Models for the remodeling of the cytoskeletal stress-fibers such as those of Deshpande et al. (2006), Vernerey and Farsad (2011) and Obbink-Huizer et al. (2014) are purely phenomenological in nature. Here we use thermodynamic considerations to motivate a model for the stress-fiber kinetics in which the observed stress, strain and strain-rate dependence of stress-fiber dynamics are natural outcomes.

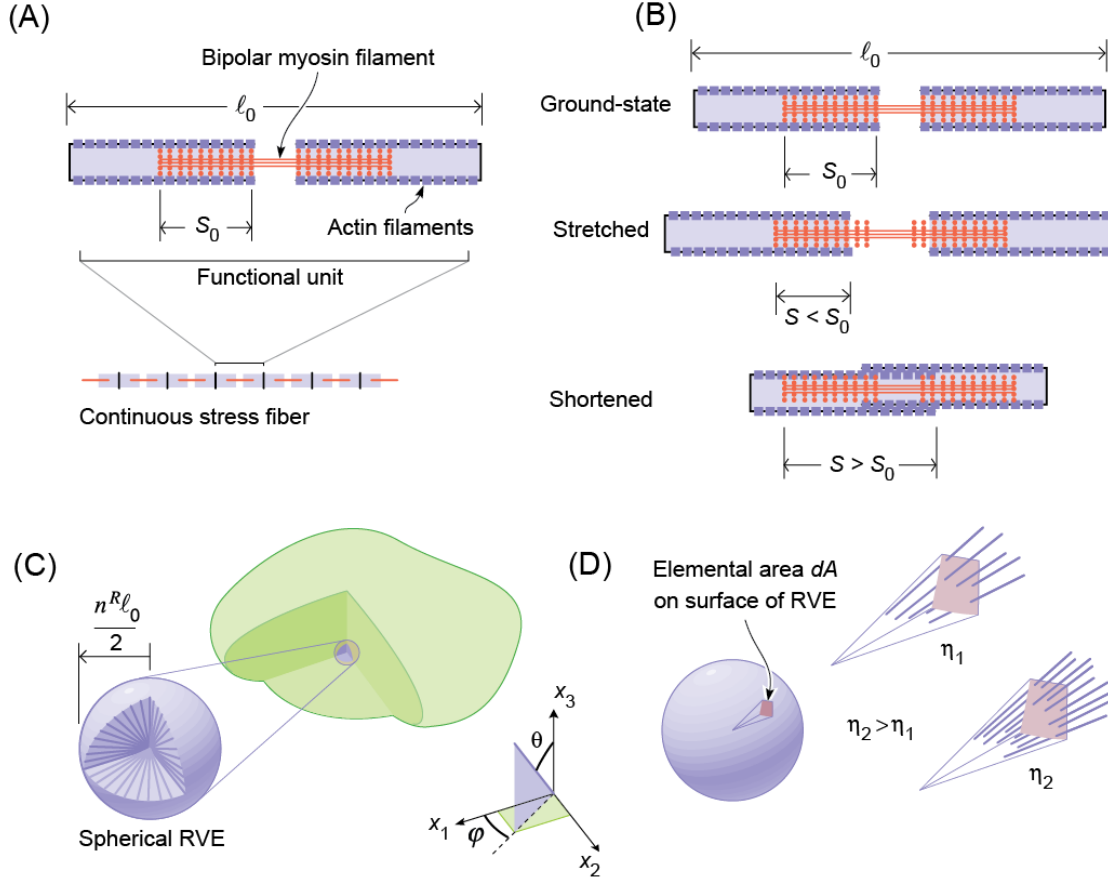


Figure 1: Sketches showing the structure of stress-fibers. (a) A single stress-fiber comprising an arrangement of functional units in series. The detailed structure of a single functional unit of the stress-fiber is included in the inset. (b) The change in the structure of the functional unit subjected to a stretch and contraction. (c) A 3D cell with a spherical RVE of radius  $n^R \ell_0 / 2$  in the undeformed setting. The inset shows the stress-fibers within the RVE. The co-ordinate system in 3D along with the definition of the angles  $(\theta, \varphi)$  are also included. (d) Sketches showing the distribution of stress-fibers within the RVE with increasing  $\eta(\theta, \varphi)$ .

### 2.1 Continuum description of stress-fibers within a cell

Contractile stress-fibers comprising proteins such as  $\alpha$ -actinin, actin, myosin and tropomyosin and showing an alternating periodic arrangement similar to that seen in muscle sarcomeres have been observed in a range of cells including endothelial cells (De Bruyn and Cho 1974), retinal cells (Gordon et al. 1982) and fibroblasts (Byers and Fujiwara 1982). We use these observations to describe the structure of stress-fibers with a view to developing a continuum model for their re-organization. Consider a single stress-fiber of cross-sectional area  $A_0$  as sketched in Fig. 1a. The fiber comprises actin filaments, myosin bipolar filaments and other proteins such as  $\alpha$ -actinin. These proteins assemble in a serial repeating manner similar to a stack of poker chips with the smallest functional unit of a stress-fiber shown in

the inset of Fig. 1a. This functional unit has a length  $\ell_0$  in its ground-state state (state with lowest internal energy) with an overlap  $s_0$  between the actin and myosin filaments. Immunofluorescence experiments by Langanger et al. (1986) suggest that  $\ell_0 \approx 0.4 \mu\text{m}$  in chicken fibroblasts. The isometric tension that the functional unit can exert is maximum in this ground-state and reduces as the functional unit is strained away from this ground state. When the functional unit is stretched, the overlap between the myosin and actin filaments decreases while when it is shortened the actin filaments interfere with each other which results in some myosin cross-bridges losing their ability to interact with the actin filaments. Both these effects are illustrated in Fig. 1b.

The aim here is to develop a continuum description of stress-fiber distributions within the cell. With this in mind, we now proceed to define volume-averaged quantities over a representative volume element (RVE). The RVE in the undeformed state is assumed to be a sphere of radius  $n^R \ell_0 / 2$  as illustrated in Fig. 1c with stress-fiber emanating from the center of this sphere. Thus, each stress-fiber within the undeformed RVE comprises  $n^R$  functional units in their ground-state. The RVE by definition is required to be large compared to the functional unit length  $\ell_0$  so as to smooth over statistical fluctuations. Moreover, we assume that the properties at each material point  $x_i$  within the cell are representative of those of the RVE and thus we implicitly assume that the property variations over the cell are occurring over wavelengths large compared to  $n^R \ell_0$ .

Now consider a material point located at  $x_i$  with the RVE describing the details of the stress-fiber structure at this point. Recall that stress-fibers crisscross the RVE such that they all pass through the center of the RVE. The unit outward normal to an infinitesimal area  $dA$  on the surface of the undeformed RVE is given by  $m_i \equiv [\sin\theta\cos\varphi \quad \sin\theta\sin\varphi \quad \cos\theta]$ , where  $\theta$  and  $\varphi$  are the polar and azimuthal angles, respectively as defined in Fig. 1c. We then define an angular stress-fiber concentration  $\eta(\theta, \varphi)$  such that  $d\Pi \equiv \eta \sin\theta d\theta d\varphi$ , where  $d\Pi$  is the number of stress-fibers passing through  $dA$  and  $\sin\theta d\theta d\varphi$  the differential solid angle subtending  $dA$ . Then the total number of stress-fibers at location  $x_i$  follows as

$$\Pi = \int_{-\pi/2}^{\pi/2} \int_0^{\pi} \eta \sin\theta d\theta d\varphi. \quad (2.1)$$

Sketches showing the distribution of stress-fibers within the RVE with increasing  $\eta(\theta, \varphi)$  are included in Fig. 1d to give a visual sense of the definition of  $\eta$ .

We now proceed to define the material strains and the strains that the stress-fiber functional units are subjected to relative to their ground-state. Assume that a nominal tensile strain  $\varepsilon_n(\theta, \varphi)$  is imposed instantaneously on the surface of the undeformed RVE normal to  $dA$  (i.e. a step change in the strain). This imposed strain causes a reduction in the overlap  $s$  between the actin and myosin filaments (i.e.  $s < s_0$ ) within the functional units of the stress-fibers oriented at  $(\theta, \varphi)$  as illustrated in Fig. 2. The functional units of the stress-fiber are now no longer in their ground-state and some cross-bridges from the bipolar myosin filament now are unable to interact with the actin filaments. This configurational change of the functional unit can be thought of as creating new surface within the unit, which in turn increases its internal energy. The increase in the internal energy of the functional unit is expected to initiate a remodeling process within the stress-fibers. In the case of an imposed stretch, the remodeling will normally involve the addition of functional units, as illustrated schematically in Fig. 2, in an attempt to increase the overlap  $s$  back to  $s_0$ . The opposite effect

occurs if  $\varepsilon_n(\theta, \varphi)$  is a compressive strain with the stress-fiber now undergoing remodeling, which involves the dissociation of functional units, such that the functional units can elongate back to near their optimal length.

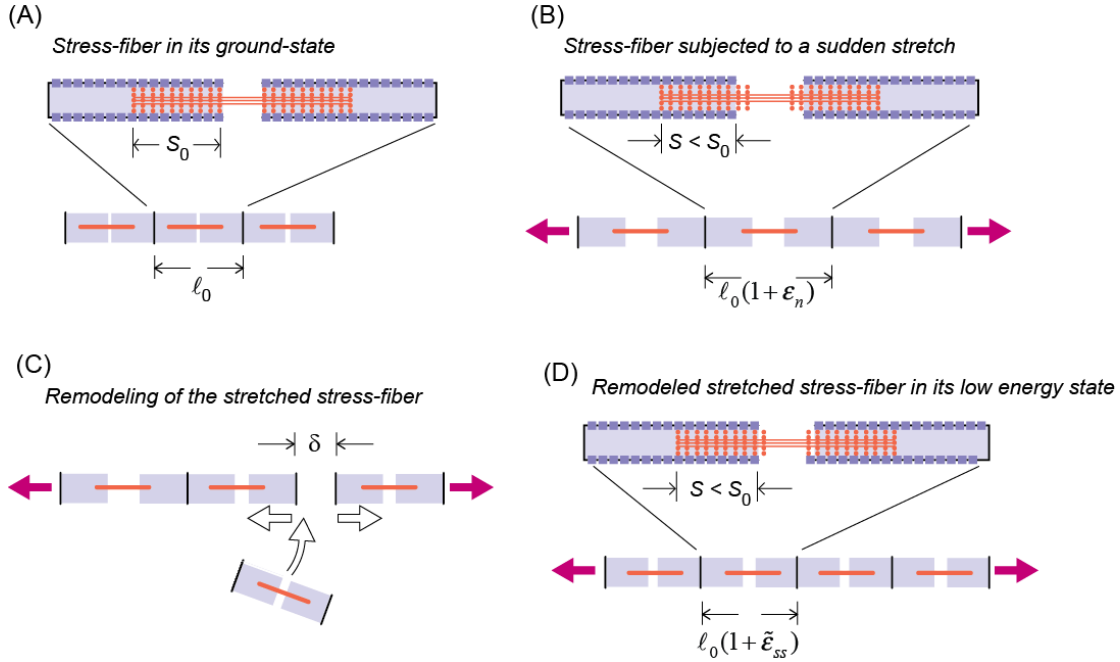


Figure 2: The remodeling of a stress-fiber subjected to a nominal tensile strain  $\varepsilon_n$ . (a) The stress-fiber in its initial ground state with an actin/myosin filament overlap  $s = s_0$  corresponding to  $\tilde{\varepsilon}_n = 0$ . (b) Stress-fiber subjected to a tensile strain  $\varepsilon_n$  which decreases the overlap to  $s < s_0$ . (c) The remodeling of the stress-fiber by the contraction of two function units and the breaking of the bond between these two units. (d) The remodeled stress-fiber where an additional functional unit is inserted into the fiber such that the fiber is now in its low energy state with each functional unit strained to  $\tilde{\varepsilon}_n^{SS}$ .

Thus, when all the functional units within each stress-fiber in the bundle with orientation  $(\theta, \varphi)$  have an overlap  $s = s_0$  there are  $n^0 \equiv n^R[1 + \varepsilon_n(\theta, \varphi)]$  functional units within the RVE in direction  $(\theta, \varphi)$  but in general the stress-fiber comprises  $n \neq n^0$  functional units. Based on this discussion, we define two strain quantities at orientation  $(\theta, \varphi)$ : (i) the material nominal strain  $\varepsilon_n(\theta, \varphi)$  which directly gives the overall change of length of a stress-fiber in direction  $(\theta, \varphi)$  and (ii) the nominal strain  $\tilde{\varepsilon}_n(\theta, \varphi)$  of the stress-fiber functional unit relative to its ground-state. The length of a functional unit in a stress-fiber comprising  $n$  functional units is  $n^0 \ell_0 / n$  and consequently  $\tilde{\varepsilon}_n$  and  $\varepsilon_n$  are related via

$$\tilde{\varepsilon}_n = \frac{n^0}{n} - 1 = \frac{n^R[1 + \varepsilon_n]}{n} - 1, \quad (2.2)$$

so that  $\tilde{\varepsilon}_n = 0$  corresponds to a functional unit in its ground-state with an actin/myosin filament overlap  $s = s_0$  and length  $\ell_0$ . **In summary,  $\eta$  quantifies the number of stress-fibers in parallel at a particular orientation while  $n$  gives the number of functional units in series within each of those stress-fibers.**

To complete the description of the continuum quantities used to define the stress-fiber structure we note that the total number of functional units within stress-fibers in the RVE at location  $x_i$  is given by

$$N_b = \int_{-\pi/2}^{\pi/2} \int_0^{\pi} \eta n \sin\theta d\theta d\varphi. \quad (2.3)$$

Further, at  $x_i$  are also present unbound actin, myosin proteins and other proteins that can combine to form  $N_u$  functional units. Therefore, the number of stress-fiber functional units that can exist within the RVE at  $x_i$  if all the available proteins combined to form functional units is

$$N_T = N_b + N_u. \quad (2.4)$$

The corresponding volumetric concentrations of these total and unbound stress-fiber protein packets are then given as

$$\rho_T \equiv \frac{N_T}{J \frac{4\pi}{3} (n^R \ell_0 / 2)^3} \quad \text{and} \quad \rho_U \equiv \frac{N_u}{J \frac{4\pi}{3} (n^R \ell_0 / 2)^3}, \quad (2.5)$$

respectively, where  $J$  is the Jacobian of the deformation gradient at  $x_i$  and  $V_R \equiv \frac{4\pi}{3} (n^R \ell_0 / 2)^3$  is the undeformed RVE volume.

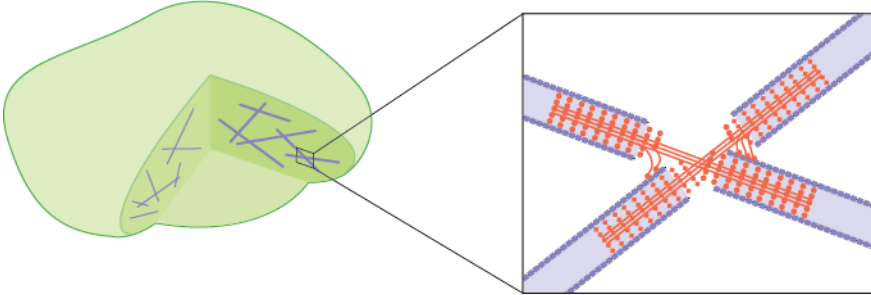


Figure 3: Stress-fibers in multiple directions in a 3D cell. The inset shows the dis-organized structure of the functional unit at the intersection between two stress-fibers in different directions: cross-bridges from myosin filaments in one stress-fiber interacting with actin filaments in the other fiber and vice-versa.

In the above discussion we have implicitly assumed that the structure of the stress-fibers is not affected by fibers at multiple orientations at any given location. However, interaction between stress-fibers in different directions is expected. To illustrate this consider stress-fibers in the 3D cell as shown in Fig. 3. The structure of the filaments within the functional units is shown in more detail in the inset of Fig. 3. Clearly cross-bridges can now form between myosin and actin filaments in different directions. This will tend to destabilize the stress-fibers and thus we argue that the structure of stress-fibers favors unidirectional fibers.

## 2.2 Development of the constitutive model

The bio-chemo-mechanical model of Deshpande et al. (2006) captures the formation and dissociation of stress-fibers, as well as the associated generation of tension and contractility. In the model, polymerization (leading to stress-fiber formation in the cell) is governed by

three coupled phenomena: (i) an activation signal, (ii) tension-dependent stress-fiber kinetics, and (iii) a force generation mechanism governed by cross-bridge cycling between actin and myosin filaments. Here we present a model (in a finite strain setting) based on this generic framework but with three critical differences:

- (a) Conservation of the stress-fiber proteins and the diffusion of the unbound proteins within the cell is considered.
- (b) Two kinetics processes are involved in the stress-fiber dynamics: the kinetics of stress-fiber formation and dissociation as well as the kinetics of stress-fiber remodeling involving the change in the number of functional units within existing stress-fibers.
- (c) All these kinetics are motivated by considering the energy levels of the proteins in their different states rather than purely phenomenological relations.

Over the time-scales being modeled here, we assume that there is negligible production or destruction of the stress-fiber proteins and thus  $\rho_T$  integrated over the entire cell volume is a conserved quantity. Thus, we define a conserved quantity

$$N_0 \equiv \frac{4\pi}{3} (n^R \ell_0/2)^3 \int_V \rho_T dV, \quad (2.6)$$

where  $V$  and  $V_0$  are the current and undeformed volumes of the entire cell, respectively. Then we introduce normalizations with respect to  $n^R$  and  $N_0$  such that

$$\widehat{N}_u + \widehat{N}_b = \widehat{N}_T, \quad (2.7)$$

where  $\widehat{N}_u \equiv N_u/N_0$ ,  $\widehat{N}_T \equiv N_T/N_0$  and

$$\widehat{N}_b \equiv \frac{N_b}{N_0} = \int_{-\pi/2}^{\pi/2} \int_0^\pi \hat{\eta} \hat{n} \sin\theta d\theta d\varphi. \quad (2.8)$$

Here,  $\hat{\eta} \equiv \eta n^R/N_0$  and  $\hat{n} \equiv n/n^R$  and consequently the normalized number of stress-fibers  $\widehat{\Pi}$  is analogously defined as

$$\widehat{\Pi} \equiv \Pi n^R/N_0 = \int_{-\pi/2}^{\pi/2} \int_0^\pi \hat{\eta} \sin\theta d\theta d\varphi. \quad (2.9)$$

With the appropriate continuum quantities now defined, we proceed to present the different elements of the constitutive model which include:

- (I) The kinetics of stress-fiber formation and dissociation.
- (II) The kinetics of stress-fiber remodeling.
- (III) Transport of the unbound stress-fiber proteins.
- (IV) The activation signal.
- (V) Force generation within the stress-fiber.
- (VI) Homogenization of the stress-fiber forces to provide a cell level constitutive relation.

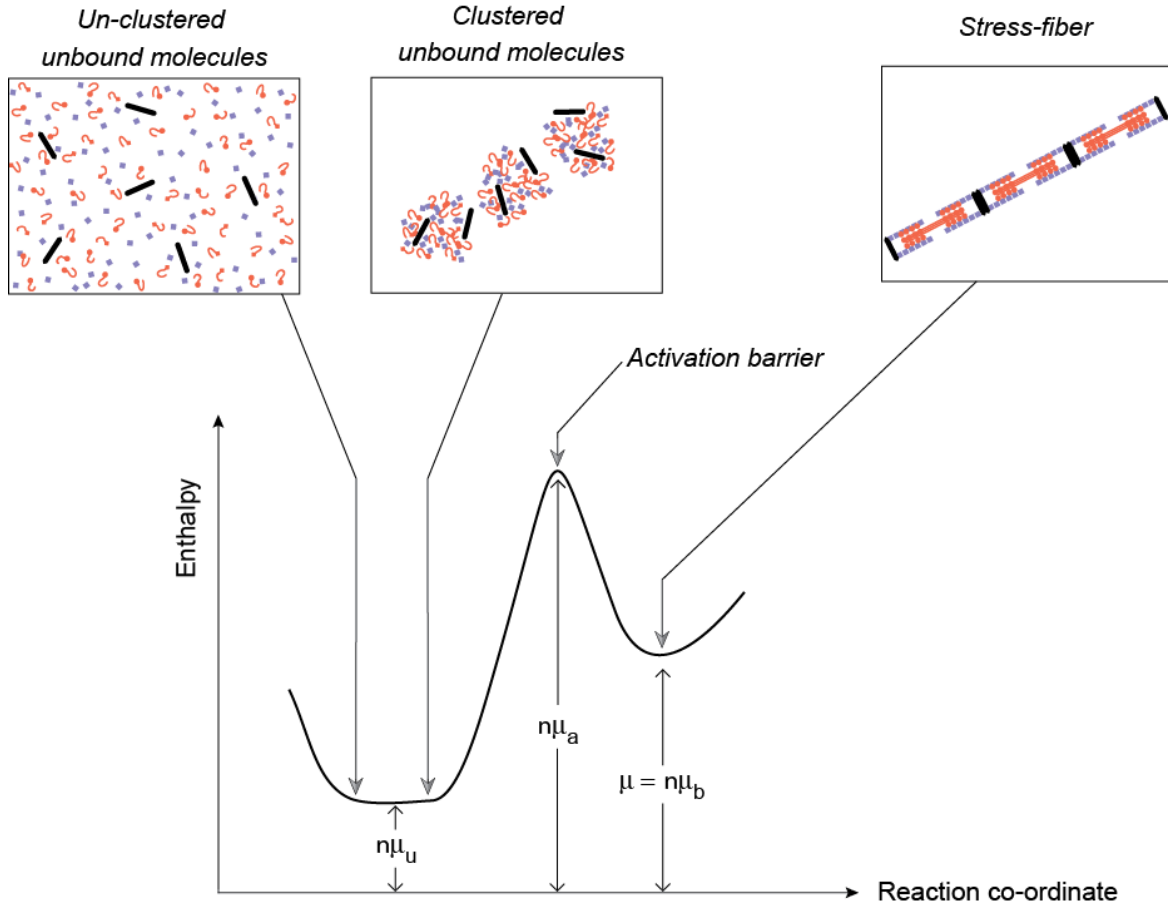


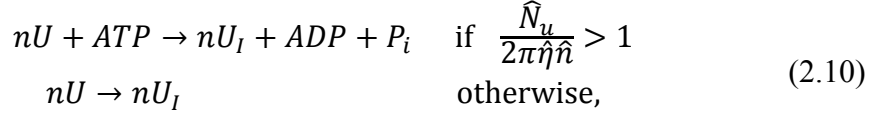
Figure 4: The energy landscape of the stress-fiber proteins ( $n^R = 1$ ). The sketch shows the standard enthalpies of the un-clustered unbound proteins, 1 packet of clustered (intermediate stage) unbound proteins that comprises aggregates to form 3 functional units and the stress-fiber comprising  $n = 3$  functional units that forms from this 1 packet. The activation barrier between the clustered unbound proteins and the bound proteins within the stress-fiber is also indicated.

### (I) Stress-fiber kinetics

Let  $\mu_b(\theta, \varphi)$  denote the standard enthalpy of  $n^R$  functional units within a stress-fiber at an orientation  $(\theta, \varphi)$  in the RVE. Then the standard enthalpy  $\mu(\theta, \varphi)$  of a stress-fiber at orientation  $(\theta, \varphi)$  comprising  $n(\theta, \varphi)$  functional units is  $\mu(\theta, \varphi) = \hat{n}\mu_b$ . The corresponding standard enthalpy of the aggregated unbound stress-fiber proteins that combine to form  $n^R$  functional units is denoted as  $\mu_u$ .

First consider the forward reaction (formation of stress-fibers) where unbound proteins combine to form a stress-fiber comprising  $n$  functional units at an orientation  $(\theta, \varphi)$ . We assume that unbound proteins are equally available to form stress-fibers at any orientation and thus  $N_u/(2\pi)$  unbound molecules are available. The geometrical arrangements of functional units within a stress-fiber bundle constrain all stress-fibers in a bundle at a particular orientation to have the same number of functional units. We thus postulate that the formation of stress-fibers proceeds in two steps. First the unbound aggregates of proteins cluster into  $N_u/(2\pi n)$  packets and each of these packets comprise molecules to form  $n$  functional units (the intermediate stage); see Fig. 4. At this intermediate stage there is no change in the enthalpy of the unbound proteins but there may be an entropy change due to the arrangement of the molecules; see Appendix A for a statistical mechanics discussion on the entropy of this intermediate stage. The clustering reaction is driven by the hydrolysis of *ATP*

into  $ADP$  and a phosphate ion  $P_i$  in case the reaction is endergonic and spontaneous in case it is exergonic, i.e.



where  $U$  and  $U_I$  denote the un-clustered unbound proteins and the clustered unbound proteins (intermediate stage), respectively<sup>1</sup>. (The condition that governs whether the clustering reaction is endergonic/exergonic is derived in Appendix A.) Second, all the  $n$  aggregates within a packet of the clustered proteins need to cross an activation enthalpy barrier (we assume that the number of energy states available to the activated state is equal to those of the unbound molecules in the intermediate state and thus the activation free-energy is equal to the activation enthalpy). This barrier is  $(\mu_a - \mu_u)$  for the formation of  $n^R$  functional units bound within a stress-fiber as depicted in Fig. 4 and the reaction is written as



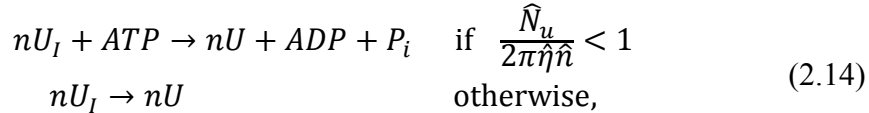
where  $B$  denotes bound functional units. Since reaction (2.10) is either  $ATP$  driven or spontaneous with no barrier, we assume that the second step, i.e. reaction (2.11) is rate limiting. The Boltzmann distribution specifies that the probability for a single aggregate of unbound molecules to cross the activation barrier is

$$k_+ = \exp\left[-\frac{\mu_a - \mu_u}{n^R k_B T}\right], \quad (2.12)$$

and the joint probability for the entire packet of  $n$  aggregates of unbound molecules to cross the activation barrier is  $k_f \equiv (k_+)^n$ . The rate of the forward reaction for the formation of the stress-fibers is then

$$r_f \equiv \frac{N_u}{2\pi n} \omega_n k_f = \frac{N_u}{2\pi n} \omega_n \exp\left[-\hat{n} \frac{\mu_a - \mu_u}{k_B T}\right], \quad (2.13)$$

where  $\omega_n$  is the collision frequency of the unbound molecules including any steric effects. Now consider the reaction for the dissociation of a stress-fiber with  $n$  functional units (reverse reaction). This again proceeds in two steps first via reaction (2.11) and then via the conversion of the clustered unbound proteins to their un-clustered state via



where the first of reaction (2.14) occurs when un-clustering is endergonic and the second case

---

<sup>1</sup>  $ATP$  hydrolysis driving the growth of actin filaments (F-actin) from the polymerisation of G-actin monomers is widely accepted; see for example Howard (2001). The reaction (2.10) is motivated from these understanding.

in case un-clustering is exergonic. Again we assume that reaction (2.11) is rate limiting, as the proteins need to cross the activation barrier  $\hat{n}(\mu_T - \mu_b)$  depicted in Fig. 4. Using the Boltzmann distribution for the energy levels of the stress-fibers and assuming the same collision frequency as in the forward reaction, the rate of the reverse reaction is

$$r_r \equiv \eta \omega_n k_b = \eta \omega_n \exp \left[ -\hat{n} \frac{\mu_a - \mu_b}{k_B T} \right], \quad (2.15)$$

where analogous to  $k_f$ ,  $k_b$  is the probability for proteins within the stress-fiber to cross the activation barrier. The net rate  $\hat{\eta}(\theta, \varphi)$  in normalized form then follows as

$$\hat{\eta} = \frac{\hat{N}_u}{2\pi \hat{n}} \omega_n \exp \left[ -\hat{n} \frac{\mu_a - \mu_u}{k_B T} \right] - \hat{\eta} \omega_n \exp \left[ -\hat{n} \frac{\mu_a - \mu_b(\theta, \varphi)}{k_B T} \right]. \quad (2.16)$$

The chemical potentials of the proteins in the un-clustered and clustered unbound states as well as in their bound states are derived in Appendix A from statistical mechanics arguments.

It now remains to specify the forms for the standard enthalpy functionals  $\mu_u$  and  $\mu_b$ . Consider first the unbound stress-fiber proteins. These proteins are affected by the activation signal level and tend to transform into their bound states more readily when the activation signal concentration (e.g. concentration of unfolded ROCK) is increased, as discussed in Section 2.1. We model the effect of the activation signal on the standard enthalpy of the unbound stress-fiber proteins via the phenomenological relation

$$\mu_u = \mu_{u0} + \Delta\mu_{u0} C, \quad (2.17)$$

where following Deshpande et al. (2006), we model the activation signal via a non-dimensional measure such that  $0 \leq C \leq 1$ ,  $\mu_{u0}$  is the standard enthalpy of the unbound stress-fiber in the absence of a signal ( $C = 0$ ) and  $\Delta\mu_{u0}$  is the increase in the enthalpy of the unbound molecules at full activation ( $C = 1$ ). Next consider a stress-fiber oriented at  $(\theta, \varphi)$ , comprising  $n$  functional units within the RVE and subject to a tensile stress  $\sigma_f(\theta, \varphi)$ . The standard enthalpy  $\mu_b$  of  $n^R$  functional units within the stress-fiber is written as

$$\mu_b \equiv \psi - \sigma_f(\theta, \varphi) [1 + \tilde{\varepsilon}_n(\theta, \varphi)] \Omega. \quad (2.18)$$

We shall now discuss each of the terms on the right hand side in the above expression. The internal energy of  $n^R$  functional units within a stress-fiber is  $\psi$ . This internal energy increases as the unit is strained away from its ground-state at  $\tilde{\varepsilon}_n = 0$  and we specify a functional form for  $\psi$  as

$$\psi \equiv \mu_{bo} + \beta \mu_{bo} |\tilde{\varepsilon}_n|^p + (1 - \kappa) \Delta \mu_{bo}. \quad (2.19)$$

Here, the internal energy of  $n^R$  functional units within a stress-fiber in their ground-state is labeled  $\mu_{bo}$  while  $\beta$  and  $p$  are non-dimensional constants governing the rate of growth of  $\psi$  as the functional units are strained away from their ground-state. We emphasize that the increase in  $\psi$ , as it is strained away from its ground-state, represents an increment in the configurational energy of the functional unit due to the reduction in the ability of the actin and myosin filaments to interact. The conjugate configurational force to this energy drives the remodeling of the stress-fiber as discussed subsequently. Thus,  $\beta \mu_{bo} |\tilde{\varepsilon}_n|^p$  should not be interpreted as strain energy as there is no mechanical stress associated with this energy. The final term in the internal energy expression takes into account that functional units are destabilized by cross-bridges formed between myosin and actin filaments in different directions (see Fig. 3). We model this by increasing the internal energy of  $n^R$  functional units by  $\Delta \mu_{bo}$  in the limit of an isotropic stress-fiber distribution. The degree of isotropy of the stress-fibers is modeled via the non-dimensional parameter  $\kappa$ , such that  $0 \leq \kappa \leq 1$  with

$$\kappa \equiv \frac{\eta_{\max} - \eta_{\min}}{\eta_{\max}}, \quad \text{where} \quad \begin{aligned} \eta_{\max} &= \max\{\eta, \forall (\theta, \varphi)\} \\ \eta_{\min} &= \min\{\eta, \forall (\theta, \varphi)\}. \end{aligned} \quad (2.20)$$

Thus,  $\kappa = 0$  for an isotropic stress-fiber distribution with  $\eta_{\max} = \eta_{\min}$  and for simplicity we postulate that  $\psi$  decreases linearly with  $\kappa$ .

The second term in Eq. (2.18) represents the change in the enthalpy of the functional units due to the work done against the environment in creating the “space” to accommodate them. Consider a stress-fiber oriented at  $(\theta, \varphi)$  comprising  $n^R$  functional units and subject to a stress  $\sigma_f(\theta, \varphi)$ . With each functional unit subjected to a strain  $\tilde{\varepsilon}_n(\theta, \varphi)$  the length of this stress-fiber is  $n^R \ell_0 [1 + \tilde{\varepsilon}_n(\theta, \varphi)]$ . The change in enthalpy in creating this stress-fiber with cross-sectional area  $A_0$  is then  $-\sigma_f(\theta, \varphi) [1 + \tilde{\varepsilon}_n(\theta, \varphi)] \Omega$ , where  $\Omega \equiv A_0 n^R \ell_0$  as specified in Eq. (2.18). The standard enthalpy of a stress-fiber comprising  $n$  functional units then follows from Eqs. (2.2) and (2.18) as

$$\mu(\theta, \varphi) \equiv \hat{n} \mu_b = \hat{n} \psi - \sigma_f(\theta, \varphi) [1 + \varepsilon_n(\theta, \varphi)] \Omega. \quad (2.21)$$

### (II) Stress-fiber remodeling

Now consider the remodeling of an existing stress-fiber at orientation  $(\theta, \varphi)$  with  $n$  functional units in the RVE. Recall that the length of functional units within stress-fibers in cells at steady-state is a constant and independent of the state of the cell such as the density of stress-fibers etc. (e.g. as shown by Guterl et al. (2007) sarcomeres are approximately  $2 \mu\text{m}$  in length in heart muscles under both isometric or under cyclic shortening conditions). Based on this observation, we postulate that only changes in the internal energy of the stress-fibers at a fixed overall strain  $\varepsilon_n(\theta, \varphi)$  drive the remodeling process: inclusion of the entropy and mechanical work contributions of the free-energy of the stress-fiber would result in the steady-state functional unit length being a function of the state of the cell contrary to

observations. As discussed in Section 2.2, there are two possible remodeling scenarios involving either the addition or dissociation of functional units and we shall consider these in turn:

(i) Addition of functional units occurs when the stress-fiber can reduce its internal energy by contracting each of its constituent functional units and thereby making room for the addition of new units. As shown in Fig. 2, this addition occurs by an opening of a gap between adjacent functional units. This involves the breaking of bonds and the formation of new bonds as a new functional unit enters the gap to form the remodeled stress-fiber. This is a dissipative process with the energy required for this remodeling provided by the reduction in the internal energy of the stress-fiber.

(ii) Dissociation of functional units from a stress-fiber occurs when the stress-fiber can reduce its internal energy by extending each of its constituent functional units and thereby reducing the number of units within it. Remodeling with functional unit dissociation occurs by first a bond breaking between two functional units and then one unit extending while the other rotates away. The remodeling is complete when the extending functional unit reforms a new bond with its new neighbor and the strain within all the functional units of the stress-fiber in the RVE readjusts and equalizes. Similar to remodeling involving functional unit addition, the bond breaking and reforming process is dissipative with the energy for this process provided by the reduction in the internal energy of the stress-fiber.

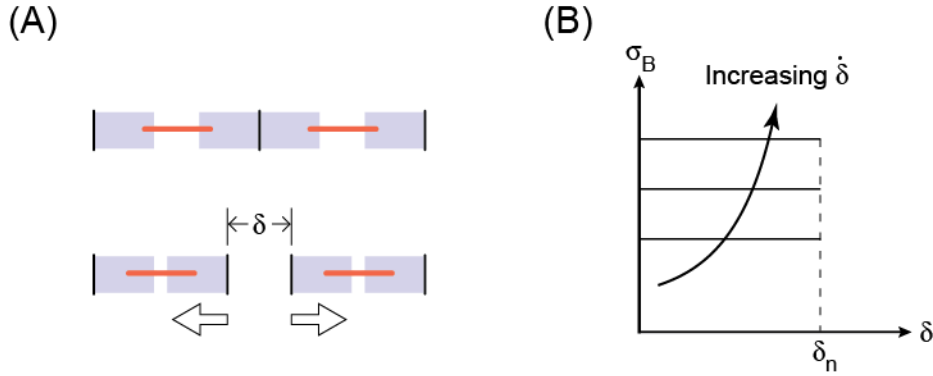


Figure 5: (a) The stretching of the bond between two functional units within a stress-fiber by  $\delta$ . (b) The variation of the bond stress  $\sigma_B$  with  $\delta$  and the stretch rate  $\dot{\delta}$ . The bonds break at a stretch  $\delta = \delta_n$ .

To develop a model for the rate  $\dot{n}$ , we first establish the rate of change of internal energy of the stress-fiber due to remodeling and then equate it to the dissipation rate due to the breakage and reformation of the bonds between the functional units. From Eqs. (2.19) and (2.2), the rate of change of the internal energy follows as

$$\dot{\Psi} = \frac{\partial \Psi}{\partial n} \dot{n} = \hat{n} \left[ \psi(\tilde{\varepsilon}_n) - \frac{\partial \psi}{\partial \tilde{\varepsilon}_n} (1 + \tilde{\varepsilon}_n) \right], \quad (2.22)$$

where  $\Psi \equiv \hat{n}\psi$ . Note that in the remodeling process the number of stress-fibers remains constant and therefore  $\eta$  (and consequently  $\kappa$ ) remain constant and thus their derivative is not included in Eq. (2.22).

We now proceed to propose a constitutive relation for the dissipation rate during the remodeling process. As a first step consider the stretching of the bond between two functional units as shown in Fig. 5a. Adhesion in most biological situations is thermally activated with

an activation barrier present for the formation/dissociation of bonds. This results in a rate dependent bond strength/energy (Evans and Ritchie, 1997). **Here we do not model these details but rather specify a simple phenomenological relation between the bond stress  $\sigma_B$  and bond stretch  $\delta$  (we do not need to consider the compression of the bond for the purposes of this discussion) that captures the key element of the rate dependence of the bond strength. This simple relation is specified by**

$$\sigma_B = \begin{cases} \frac{q \ell_0}{\delta_n} \left( \frac{\delta}{\delta_n} \right) & \text{for } \delta \leq \delta_n \\ 0 & \text{otherwise,} \end{cases} \quad (2.23)$$

where  $q \ell_0 / \delta_n$  is the bond viscosity and  $\delta_n$  the bond stretch at which the bond breaks; see Fig. 5b. Typically we would anticipate  $q$  to scale as  $q \propto [E_b / (k_B T)]$ , where  $E_b$  is the activation energy for the breaking of the bonds. This activation energy will govern the rate of stress-fiber remodeling and is strongly dependent on the cell type; e.g.  $E_b$  is expected to increase from pluripotent cells to progenitor cells to differentiated cells thereby increasing the bond viscosity and the consequently the dissipation rate during remodeling.

**The dissipation rate  $\dot{D}$  over the  $n$  junctions between functional units in the stress-fiber is given as  $\dot{D} \equiv n \sigma_B A_0 \dot{\delta}$ . If the bonds are breaking at a rate  $\dot{r}_B \equiv \dot{\delta} / \delta_n$ ,  $\dot{D}$  follows as**

$$\dot{D} \equiv n \sigma_B A_0 \dot{\delta} = n q A_0 \ell_0 \dot{r}_B^2 = \hat{n} q \Omega \dot{r}_B^2. \quad (2.24)$$

It now remains to relate  $\dot{r}_B$  to  $\dot{n}$  and we consider the cases of functional unit addition and dissociation separately. First consider the case of the addition of functional units. Let  $n_u$  functional units not within a stress-fiber (i.e. unbound functional units) be available for addition to each stress-fiber during remodeling. With  $\Pi$  stress-fibers within a RVE it is reasonable to assume that  $n_u = N_u / \Pi$ . Over the stress-fiber length in the RVE,  $n \dot{r}_B$  junctions between functional units break in unit time with  $n_u / n$  functional units available to enter each of these broken junctions. Thus,  $\dot{n} = n_u \dot{r}_B$  and the dissipation rate during the addition of functional units is given by

$$\dot{D} = \hat{n} q \Omega \left( \frac{\hat{\Pi}}{\hat{N}_u} \right)^2 \hat{n}^2. \quad (2.25)$$

Now consider the case of the dissociation of a functional unit from a stress-fiber. A functional units dissociates from the stress-fiber when the bond at both its ends breaks. Over the stress-fiber length within the RVE,  $n \dot{r}_B$  junctions between functional units break in unit time and on average we would expect  $n \dot{r}_B / 2$  functional units to dissociate implying  $\dot{n} = n \dot{r}_B / 2$ . The dissipation rate during remodeling with functional unit dissociation then follows as

$$\dot{D} = \frac{4q\Omega}{\hat{n}} \hat{n}^2. \quad (2.26)$$

The kinetic law for  $\dot{n}$  follows from the balance relationship  $-\dot{\Psi} = \dot{D}$ , i.e. the rate of loss of internal energy from the stress-fiber during remodeling is equal to the dissipation rate. Recall that  $\dot{D}$  is always positive. Therefore, from Eq. (2.22) it is clear that when  $\partial \Psi / \partial \hat{n} > 0$ ,

remodeling involves dissociation with  $\dot{n} < 0$  while remodeling results in functional unit addition with  $\dot{n} > 0$  when  $\partial\Psi/\partial\hat{n} < 0$ . Thus, combining Eqs. (2.22), (2.25) and (2.26) the kinetic law for stress-fiber remodeling is given by

$$\hat{n} = \begin{cases} -\frac{1}{\hat{n}} \left( \frac{\hat{N}_u}{\hat{\Pi}} \right)^2 \left[ \psi(\tilde{\varepsilon}_n) - \frac{\partial\psi}{\partial\tilde{\varepsilon}_n} (1 + \tilde{\varepsilon}_n) \right] \frac{\alpha}{\mu_{bo}} & \text{if } \frac{\partial\Psi}{\partial\hat{n}} \leq 0 \\ -\frac{\hat{n}}{4} \left[ \psi(\tilde{\varepsilon}_n) - \frac{\partial\psi}{\partial\tilde{\varepsilon}_n} (1 + \tilde{\varepsilon}_n) \right] \frac{\alpha}{\mu_{bo}} & \text{otherwise,} \end{cases} \quad (2.27)$$

where the rate constant  $\alpha \equiv \mu_{bo}/q\Omega$ .

Recall that remodeling terminates when  $\partial\Psi/\partial\hat{n} = 0$ . This specifies that steady-state occurs when the nominal functional unit strain attains a value  $\tilde{\varepsilon}_{ss}$  given by positive root of the relation

$$(p-1) \tilde{\varepsilon}_{ss}^p + p \tilde{\varepsilon}_{ss}^{(p-1)} - \frac{\vartheta}{\beta} = 0, \quad (2.28)$$

where  $\vartheta \equiv 1 + (1 - \kappa)\Delta\mu_{bo}/\mu_{bo}$ . Corresponding to this strain the stress-fiber at steady-state comprises

$$\hat{n}^{ss} = \frac{1 + \varepsilon_n}{1 + \tilde{\varepsilon}_{ss}}, \quad (2.29)$$

functional units.

The remodeling of stress-fibers as proposed here will result in stress-fibers losing memory to an imposed strain  $\varepsilon_n$  as the functional units relax back to  $\tilde{\varepsilon}_{ss}$ . The model thus presents a physical rationalization of the so-called fading memory models used extensively to model the active stress of cardiac and other cells (Hunter 1995).

### (III) Transport of the unbound stress-fiber proteins

To complete the constitutive equations for the concentration of the stress-fiber proteins, we need to specify the temporal evolution of  $\hat{N}_T$ . If the stress-fiber proteins are immobile within the cell then  $\dot{\hat{N}}_T = 0$  and the total number of stress-fiber proteins (unbound and within stress-fibers) are conserved at each material point  $x_i$  within the cell. However, fluorescence recovery after photo-bleaching (FRAP) measurements (McGrath et al. 1998) suggest that unbound stress-fiber proteins such as actin can diffuse a distance of about  $1.5 \mu\text{m}$  in 1 s and thus are fast relative to the time-scales typically being modeled here. Hence the transport of the stress-fiber proteins needs to be considered to evolve  $\hat{N}_T$ .

The unbound stress-fiber proteins are free to diffuse within the cell while the bound proteins are immobile as they are connected to a network of fibers that crisscross the cell. The chemical potential of the unbound stress-fiber protein packets at location  $x_i$  in the cell is given by Eq. (A5) (see Appendix A) as

$$\chi_u = k_B T \ln \left( \frac{\hat{N}_u}{2\pi \hat{N}_L} \right) + \frac{\mu_u}{n^R}, \quad (2.30)$$

where  $\hat{N}_L$  are the normalized number of available lattice sites as defined in Appendix A. The mean drift velocity of these proteins is then obtained via the constitutive equation

$$v_i = -\Theta \frac{\partial \chi_u}{\partial x_i}, \quad (2.31)$$

where  $\Theta$  is the mobility of the unbound stress-fiber proteins in the cytoplasm. The net flux of the unbound proteins  $j_i = N_u v_i$  and the conservation of both bound and unbound stress-fiber proteins at location  $x_i$  specifies

$$\dot{N}_T = -\frac{\partial j_i}{\partial x_i}. \quad (2.32)$$

Equations (2.30)-(2.32) can be combined along with the definitions (2.5) to yield the transport equation

$$\dot{\hat{N}}_T = k_B T \frac{\partial}{\partial x_i} \left[ \Theta \frac{\partial \hat{N}_u}{\partial x_i} \right] + \frac{1}{n^R} \frac{\partial}{\partial x_i} \left[ \Theta \hat{N}_u \frac{\partial \mu_u}{\partial x_i} \right]. \quad (2.33)$$

Equation (2.33) along with the appropriate initial and boundary conditions (typically zero flux of  $\hat{N}_u$  across the cell membrane) for  $\hat{N}_u$  will provide the solution of the evolution of  $\hat{N}_T$ .

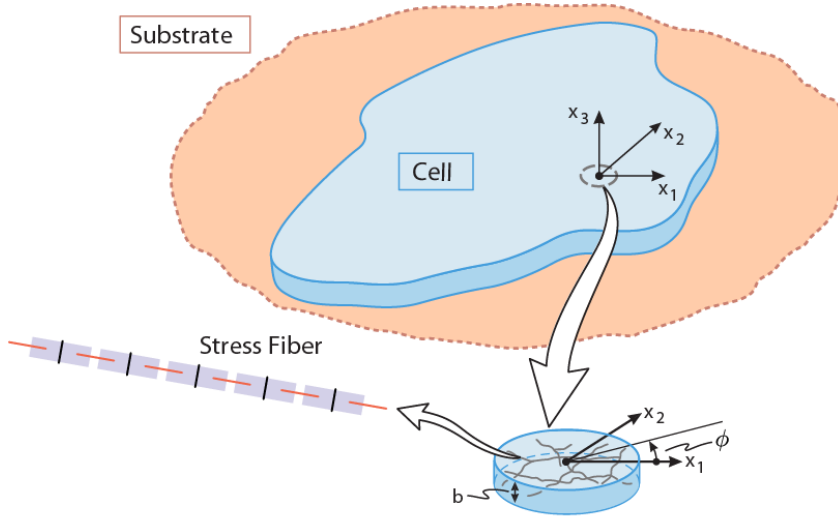


Figure 6: Schematic of a 2D cell with the co-ordinate system marked. The network of stress-fibers with the 2D RVE is shown in the inset.

#### (IV) The activation signal

Stress-fiber formation is initiated by a biochemical or mechanical perturbation that triggers a signaling cascade within the cell. We model this signal as an externally initiated, exponentially decaying pulse having level  $C$  given by

$$C = \exp\left(-\frac{t_l}{\zeta}\right), \quad (2.34)$$

where  $\zeta$  is a constant that controls the decay rate of the signal and  $t_l$  is the time measured from the instant the most recent signal is imposed. In reality, the clustering of high-affinity integrins in focal adhesions internally initiates the signaling cascade that results in the formation of stress-fibers by increasing  $C$ . The signal subsides due to restoring mechanisms that include: (i) the dephosphorylation of Rho and (ii) the refolding of ROCK into its deactivated state in the absence of the phosphorylated Rho. The complex signaling pathways that govern the rise and fall of this activation signal are neglected in this analysis, and we model the activation process due to the contact of the cell with the ligand pattern on the substrate through a pre-specified activation signal of the form given by Eq. (2.34). Readers are referred to Pathak et al. (2011) and Vigliotti et al. (2015) for more rigorous formulation for the signal  $C$  that can also be readily incorporated into this model.

#### (V) Stress-fiber force generation

Cross-bridge cycling between the actin and the myosin filaments generates the tension in the stress-fibers. This force generation mechanism is similar (but not identical) to that in muscle cells. **Here we do not model the details of the kinetics of the actin/myosin interaction (cross-bridge dynamics) which requires a consideration of kinetics at single protein length-scale (Eisenberg et al. 1980). Rather we directly specify a phenomenological expression for the relation of the stress-fiber stress to the extension/shortening rate motivated by the Hill relation (Hill, 1938).** The stress generated by the stress-fiber due to cross-bridge cycling between the actin and myosin is governed by the relative sliding rate between the actin and myosin filaments. Thus, the relevant strain-rate while considering a Hill-type relation of a single stress-fiber is the strain-rate of a functional unit within the stress-fiber rather than the overall rate of change of length of the stress-fiber. The true strain of a functional unit is related to its nominal strain via  $\tilde{\varepsilon} \equiv \ln(1 + \tilde{\varepsilon}_n)$ . Then using the definition of  $\tilde{\varepsilon}_n$  in Eq. (2.2), the true strain-rate  $\dot{\tilde{\varepsilon}}$  follows as

$$\dot{\tilde{\varepsilon}} = \frac{\dot{n}^0}{n^0} - \frac{\dot{n}}{n} = \dot{\varepsilon} - \frac{\dot{n}}{n}, \quad (2.35)$$

where again the true material strain  $\varepsilon$  is related to the corresponding nominal strain via  $\varepsilon \equiv \ln(1 + \varepsilon_n)$ . A simplified version of the Hill-like relation is then specified as

$$\frac{\sigma_f(\theta, \varphi)}{\sigma_0(\tilde{\varepsilon}_n)} = \frac{1}{2} \left[ \operatorname{erf} \left( \frac{4\dot{\tilde{\varepsilon}}(\theta, \varphi)}{\dot{\varepsilon}_0} + 2 \right) + 1 \right], \quad (2.36)$$

which is a smooth version of the piecewise linear function employed by Deshpande et al. (2006). Here  $\sigma_0$  is the isometric tension of the stress-fiber with functional units at a strain state  $\tilde{\varepsilon}_n$  and the tensile stress in the stress-fiber drops to approximately zero at a shortening rate  $\dot{\tilde{\varepsilon}} = -\dot{\varepsilon}_0$ . The isometric tension depends on the overlap  $s$  between the actin and myosin filaments with the isometric tension being a maximum at the optimum overlap  $s_0$ . Following data for muscle fibers (McMahon 1984) we propose a functional form for  $\sigma_0(\tilde{\varepsilon}_n)$  as

$$\sigma_0 = \begin{cases} \sigma_{\max} & |\tilde{\varepsilon}_n| \leq \varepsilon_p \\ \sigma_{\max} \exp \left[ - \left( \frac{|\tilde{\varepsilon}_n| - \varepsilon_p}{\varepsilon_s} \right)^2 \right] & \text{otherwise,} \end{cases} \quad (2.37)$$

where  $\sigma_{\max}$  is the isometric tension near the overlap  $s_0$  (corresponding to  $\tilde{\varepsilon}_n = 0$ ) while  $\varepsilon_p$  and  $\varepsilon_s$  govern the rate at which  $\sigma_0$  decreases as the functional unit is strained away from its ground-state. **The strain-rate and strain dependence of the stress-fiber stress as given by Eqs. (2.36) and (2.37), respectively, is sketched in Fig. 7.**

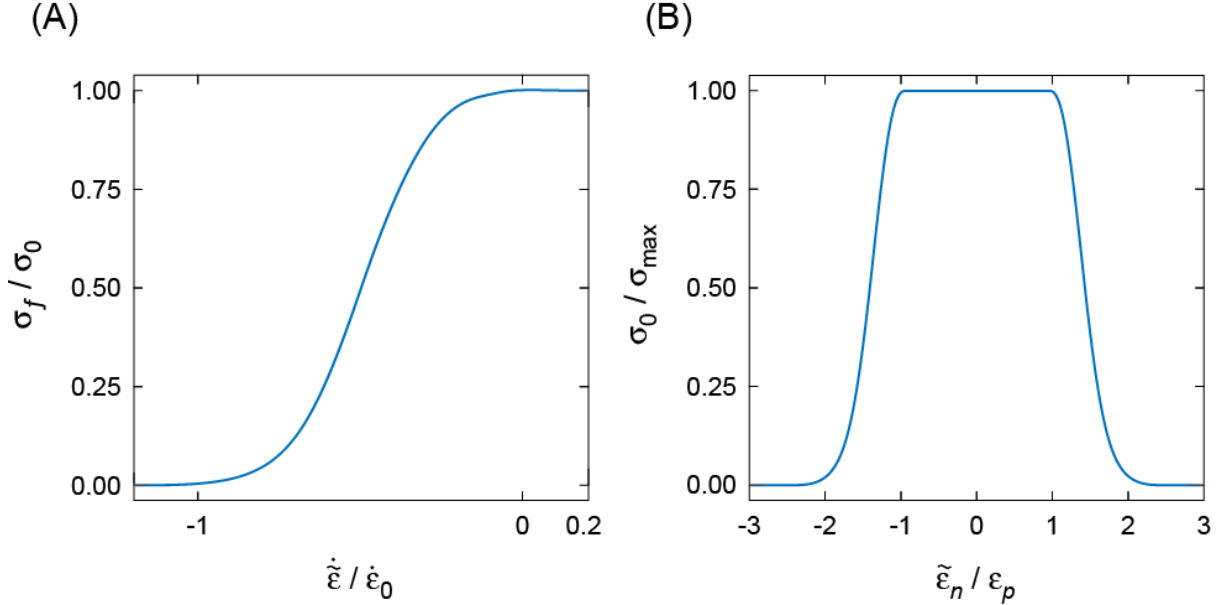


Figure 7: Sketches showing the (a) strain-rate and (b) strain dependence of the stress-fiber stress as characterized by Eqs. (2.36) and (2.37). In (b) consistent with the parameters used in this study we have assumed  $\varepsilon_p/\varepsilon_s = 2$ .

#### (VI) Homogenization and cell level constitutive relations

Consider the RVE of volume  $V$  sketched in Fig. 1c. By adopting Cartesian tensor notation (Einstein summation convention over repeated indices), the average Cauchy stress  $\sigma_{ij}$  over the RVE of volume  $V_R$  resulting from the fibers is defined from the stress  $\tau_{ij}$  at any point as

$$\sigma_{ij} = \frac{1}{V_R} \int_{V_R} \tau_{ij} dV, \quad (2.38)$$

with respect to the fixed orthogonal basis  $x_i$  (Fig. 1c). **Recall that  $\eta(\theta, \varphi)$  is the angular concentration of stress-fiber at orientation  $(\theta, \varphi)$ . We define an orthogonal set of base vectors  $e_i$  that rotate (but do not deform) with the material.** Since  $e_i$  are coincident with  $x_i$  at time  $t = 0$ ,  $(\theta, \varphi)$  gives the stress-fiber orientation in the original configuration. Now write a unit radial unit vector  $m_i = [\sin\theta\cos\varphi \quad \sin\theta\sin\varphi \quad \cos\theta]$  for the RVE so that the strain-rate in a fiber oriented at  $(\theta, \varphi)$  in the undeformed configuration is related to the material strain-rate  $\dot{\varepsilon}_{ij}$  via

$$\dot{\varepsilon}(\theta, \varphi) = \dot{\varepsilon}_{ij} m_i^* m_j^*, \quad (2.39)$$

where  $m_i^* = R_{ij}m_j$  with  $R_{ij}$  the rotation tensor at  $x_i$ . The virtual work statement for the RVE in its deformed state is then

$$\frac{1}{V_R} \int_{V_R} \tau_{ij} \delta \dot{\epsilon}_{ij} dV = \frac{1}{V_R} \int_S T_i \delta \dot{u}_i dS, \quad (2.40)$$

in terms of the traction  $T_i$  on the surface  $S$  of the deformed RVE and  $\delta \dot{u}_i$  the virtual displacement rate corresponding to the arbitrary variation  $\delta \dot{\epsilon}_{ij}$ . The current radius of the RVE at orientation  $(\theta, \varphi)$  is  $r = [1 + \epsilon_n(\theta, \varphi)] n^R \ell_0 / 2$  and  $\eta(\theta, \varphi) / r^2$  stress-fibers emanate from the RVE at orientation  $(\theta, \varphi)$  per unit deformed RVE surface area. Hence,  $T_i = \eta(\theta, \varphi) \sigma_f(\theta, \varphi) A_0 m_i^* / r^2$  while  $\delta \dot{u}_i = r \delta \dot{\epsilon}(\theta, \varphi) m_i^*$ . Substituting these into Eq. (2.40) with  $dS = r^2 \sin \theta d\theta d\varphi$  gives

$$\begin{aligned} & \frac{1}{V_R} \int_{V_R} \tau_{ij} \delta \dot{\epsilon}_{ij} dV = \\ & \frac{A_0 \ell_0 n^R}{J \frac{4\pi}{3} (n^R \ell_0 / 2)^3} \int_{-\pi/2}^{\pi/2} \int_0^\pi \eta(\theta, \varphi) \sigma_f(\theta, \varphi) [1 + \epsilon_n(\theta, \varphi)] \delta \dot{\epsilon}(\theta, \varphi) \sin \theta d\theta d\varphi. \end{aligned} \quad (2.41)$$

Combining Eq. (2.41) with Eqs. (2.38) and (2.39) specifies

$$\begin{aligned} & \sigma_{ij} \delta \dot{\epsilon}_{ij} = \\ & \frac{\hat{\sigma}_{\max}}{J} \int_{-\pi/2}^{\pi/2} \int_0^\pi \hat{\eta}(\theta, \varphi) \hat{\sigma}_f(\theta, \varphi) [1 + \epsilon_n(\theta, \varphi)] \delta \dot{\epsilon}_{ij} m_i^* m_j^* \sin \theta d\theta d\varphi, \end{aligned} \quad (2.42)$$

where  $\hat{\sigma}_f \equiv \sigma_f / \sigma_{\max}$  and  $\hat{\sigma}_{\max} \equiv f_0 \sigma_{\max}$  with the volume fraction  $f_0$  defined as

$$f_0 \equiv \frac{A_0 \ell_0 N_0}{\frac{4\pi}{3} \left( \frac{n^R \ell_0}{2} \right)^3}. \quad (2.43)$$

Recall that  $\delta \dot{\epsilon}_{ij}$  is an arbitrary variation in  $\dot{\epsilon}_{ij}$ . Thus, by successively allowing one component of  $\delta \dot{\epsilon}_{ij}$  to be non-zero while the others are set to zero, the average stress  $\sigma_{ij}$  due to the stress-fibers at location  $x_i$  is given a

$$\sigma_{ij} = \frac{\hat{\sigma}_{\max}}{J} \int_{-\pi/2}^{\pi/2} \int_0^\pi \hat{\eta} \hat{\sigma}_f [1 + \epsilon_n(\theta, \varphi)] m_i^* m_j^* \sin \theta d\theta d\varphi. \quad (2.44)$$

The total stress  $\Sigma_{ij}$  is expected to include a contribution from the passive elasticity provided mainly by the intermediate filaments of the cytoskeleton attached to the nuclear and plasma membranes and the microtubules. Here, for simplicity, we employ a neo-Hookean elasticity model with a strain energy density function given by

$$W = \frac{E}{4(1+\nu)} \left[ J^{-2/3} \sum_{j=1}^3 \lambda_j^2 - 3 \right] + \frac{E}{6(1-2\nu)} [J - 1]^2, \quad (2.45)$$

where  $\lambda_i$  are the three principal stretches with  $J \equiv \lambda_1 \lambda_2 \lambda_3$  while  $E$  and  $\nu$  are the Young's modulus and Poisson's ratio, respectively. The associated principal Cauchy stresses are

$$\sigma_i^p \equiv \frac{\lambda_i}{J} \frac{\partial W}{\partial \lambda_i}. \quad (2.46)$$

The total Cauchy stress  $\Sigma_{ij}$  follows from an additive decomposition as

$$\Sigma_{ij} = \sigma_{ij} + \sigma_{ij}^p, \quad (2.47)$$

where  $\sigma_{ij}^p$  is the passive Cauchy stress such that  $\sigma_{ki}^p p_l^{(i)} = \sigma_i^p p_l^{(i)}$  with  $p_l^{(i)}$  being unit vectors in the principal directions.

The specification for the constitutive model is completed by requiring that mechanical equilibrium is satisfied, i.e.

$$\frac{\partial \Sigma_{ij}}{\partial x_j} = 0, \quad (2.48)$$

subject to the appropriate displacement and traction boundary conditions.

#### 2.4 Specialization to a two-dimensional (2D) state

The model developed above can be readily specialized to a 2D state for a planar cell as sketched in Fig. 6 by setting  $\theta = \pi/2$  and defining an in-plane fiber orientation  $\phi = \varphi$  as shown in Fig. 6. Here we briefly summarize the key elements of the 2D formulation. The main difference between the 2D and 3D formulation lies in the RVE definition. In 2D the RVE is a cylinder of radius  $n^R \ell_0/2$  and height  $b$  in the undeformed configuration. Using the RVE sketched in Fig. 6, the stress-fiber orientation in the undeformed configuration is described by the angle  $\phi$  that varies over  $-\pi/2 \leq \phi \leq \pi/2$  and the RVE comprises  $n_s$  identical stress-fiber layers through the thickness  $b$ . Similar to the 3D case, we measure the orientation  $\phi$  of the stress-fibers with respect to an orthogonal set of base vectors  $e_i$  that rotate (but do not deform) with the material with  $e_i$  are coincident with  $x_i$  at time  $t = 0$ . The angular concentrations of the stress-fibers is now  $\eta(\phi)$  and the analogous to Eq. (2.4) the total number of functional units that can exist at a location  $x_i$  is written as

$$\hat{N}_u + \int_{-\pi/2}^{\pi/2} \hat{\eta} \hat{n} d\phi = \hat{N}_T, \quad (2.49)$$

with the total number of stress-fibers given by

$$\hat{\Pi} = \int_{-\pi/2}^{\pi/2} \hat{\eta} d\phi. \quad (2.50)$$

The stress-fiber kinetic relation Eq. (2.16) is modified as

$$\dot{\hat{\eta}} = \frac{\hat{N}_u}{\pi \hat{n}} \omega_n \exp \left[ -\hat{n} \frac{\mu_a - \mu_u}{k_B T} \right] - \hat{\eta} \omega_n \exp \left( -\hat{n} \frac{\mu_a - \mu_b(\phi)}{k_B T} \right), \quad (2.51)$$

while the stress-fiber remodeling relation remains unchanged. In 2D, the relation for the stress-fiber strain  $\hat{\varepsilon}(\phi)$  can be simply written in terms of  $\hat{\varepsilon}_{ij}$  as

$$\dot{\varepsilon}(\phi) = \dot{\varepsilon}_{11} \cos^2 \phi^* + \dot{\varepsilon}_{22} \sin^2 \phi^* + \dot{\varepsilon}_{12} \sin 2\phi^*, \quad (2.52)$$

where  $\phi^*$  is the angle of the stress-fiber measured with respect to  $x_i$  and is related to  $\phi$  by the rotation of the base vectors  $e_i$ . The 2D stress-state due to the stress-fibers of then follows from the homogenization analysis as

$$\begin{bmatrix} \sigma_{11} & \sigma_{12} \\ \sigma_{12} & \sigma_{22} \end{bmatrix} = \frac{\hat{\sigma}_{\max}}{J} \int_{-\pi/2}^{\pi/2} \hat{\eta} \hat{\sigma}_f [1 + \varepsilon_n(\phi)] \begin{bmatrix} \cos^2 \phi^* & \frac{\sin 2\phi^*}{2} \\ \frac{\sin 2\phi^*}{2} & \sin^2 \phi^* \end{bmatrix} d\phi, \quad (2.53)$$

where again  $\hat{\sigma}_{\max} \equiv f_0 \sigma_{\max}$  and the volume fraction  $f_0$  in this 2D setting is defined as

$$f_0 \equiv \frac{A_0 \ell_0 N_0}{\frac{\pi b}{n_s} \left( \frac{n^R \ell_0}{2} \right)^2}. \quad (2.54)$$

The passive stress is given by the neo-Hookean elasticity model described above: in this 2D setting we assume plane stress conditions so that  $\Sigma_{33} = 0$  with  $\sigma_3^p = 0$ . **A summary of the key parameters of the model with a brief description of each of those parameters is given in Table 1.**

<b>Parameter symbol</b>	<b>Brief description</b>
$\eta$	angular concentration of stress-fibers at orientation $(\theta, \varphi)$
$A_0; \Omega$	cross-sectional area of stress-fiber; volume of $n^R$ functional units of the stress-fiber.
$\ell_0$	undeformed length of a functional unit.
$n; n^0; n^R$	number of functional units within a stress-fiber; number of functional units within stress-fiber when functional unit strain $\tilde{\varepsilon}_n = 0$ ; reference number of functional units within the stress-fiber in an undeformed RVE.
$\varepsilon_n$	nominal strain of a stress-fiber.
$\tilde{\varepsilon}_n$	nominal strain of the functional units within a stress-fiber.
$n^{ss}; \tilde{\varepsilon}_{ss}$	number of functional units in stress-fiber at steady-state; the functional unit strain at steady-state
$N_T; N_b; N_u$	total number of protein packets in an RVE; number of protein packets in the form of bound functional units in an RVE ; number of unbound protein packets in an RVE.
$\Pi$	total number of stress-fibers within an RVE.
$\mu_a; \mu_u; \mu_b$	activation enthalpy for $n^R$ protein packets; enthalpy of $n^R$ protein packets in the unbound state; enthalpy of $n^R$ protein packets in bound state.

$\mu_{uo}; \mu_{bo}$	standard enthalpy of $n^R$ functional units in the unbound and bound states.
$\omega_n$	frequency of molecular collisions.
$C$	normalized activation signal strength ( $0 \leq C \leq 1$ ).
$\psi$	internal energy of $n^R$ functional units within a stress-fiber.
$q$	viscosity of the bond between functional units in a stress-fiber.
$\dot{D}$	dissipation rate during remodeling of a stress-fiber.
$\Theta$	mobility of the unbound stress-fiber proteins within the cytoplasm.
$\sigma_{max}$	maximum tensile stress of a stress-fiber.
$\sigma_f$	stress-fiber stress.
$\Sigma_{ij}; \sigma_{ij}; \sigma_{ij}^p$	total Cauchy stress; active Cauchy stress; passive Cauchy stress
$\kappa$	parameter characterizing the isotropicity of the distribution of stress-fibers with an RVE.

Table 1: A summary of the key parameters of the model.

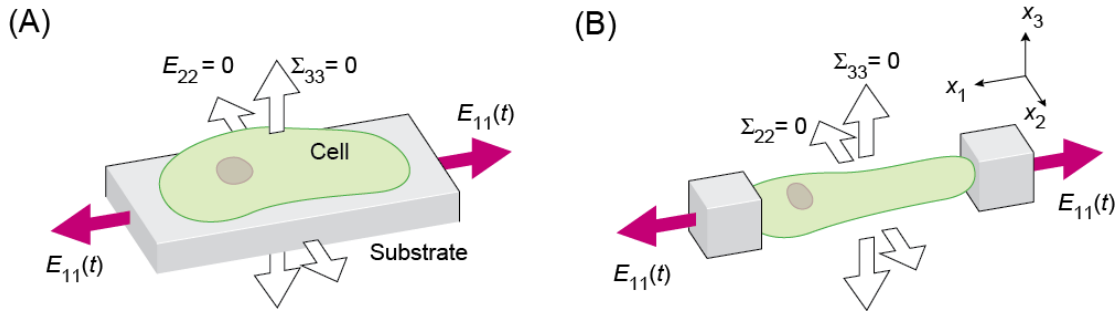


Figure 8: Sketches of the cyclic loading of cells (a) cultured on 2D stiff substrates (type I experiments) and (b) constrained within a 3D matrix or gel (type II experiments).

### 3. Simulation of cyclic stretch

Experiments wherein cells have been subjected to cyclic stretching have typically been performed under two types of conditions:

*Type I* (cells cultured on 2D substrates): As sketched in Fig. 8a, cells are cultured on flat substrates that are stiff compared to the cells. These substrates are then subjected to cyclic stretch in one direction and constrained from contraction in the orthogonal in-plane direction.

*Type II* (cells constrained in 3D tissues): Cells are cultured in a 3D matrix or gel (Fig. 8b). Left unconstrained this gel then compacts in all directions due to the contractile forces exerted by the stress-fibers and the stress-fiber distribution is isotropic. These tissues are subjected to cyclic stretch in one direction and left unconstrained (i.e. free to contract) in the other two orthogonal directions.

Here we attempt to use the model developed in Section 2 to predict the response of cells subject to cyclic loading in the type I and II experiments.

### 3.1 Simulation procedure

The cells under both type I and type II loading conditions are subjected to stretch in the  $x_1 - x_2$  plane as shown in Fig. 8 and free to contract in the  $x_3 -$  direction. Thus, the stress-fiber density out of the  $x_1 - x_2$  plane is negligible and this was confirmed via a few representative 3D calculations. Moreover, experimental observations typically only visualize the stress-fibers in the  $x_1 - x_2$  plane. Hence, here we only present results using the 2D version of the model detailed in Section 2, i.e. only considering stress-fibers in the  $x_1 - x_2$  plane. The critical difference between experiments of Type I and II lies in the boundary conditions imposed on the cells and here we describe each of these in turn.

*Simulations of Type I experiments:* The problem under consideration entails the cyclic loading of cells adhered to (typically) silicone substrates (Fig. 8a). The cyclic loads are applied to the substrate and the imposed strains measured by imaging the displacements of particles attached to the substrate. We idealize the experimental situation by making two assumptions:

- (i) The focal adhesions between the substrate and the cells are strong enough that the cell is firmly attached to the substrate and undergoes straining equal to that of the substrate.
- (ii) The in-plane strains in the cell are spatially uniform, consistent with experimental observations; see for example Neidlinger-Wilke et al. (2001).

With the cells subjected to a spatially uniform state,  $\hat{N}_T = 1$  throughout the cell and  $\hat{N}_T = 0$ , i.e. the solution of Eq. (2.33) is trivial. Moreover, the mechanical boundary conditions reduce to imposing a stress and strain state rather than displacement and/or traction boundary conditions. In the 2D simulations presented here, we apply a spatially uniform time-dependent nominal strain  $E_{11}(t)$  and  $E_{22} = E_{12} = 0$  to the cell. In addition we impose plane stress conditions in the  $x_3$ -direction such that  $\Sigma_{33} = 0$  which in this 2D case reduces to  $\sigma_{33}^p = \sigma_{33} = 0$  and  $E_{33}$  directly follows from the elastic constitutive relation.

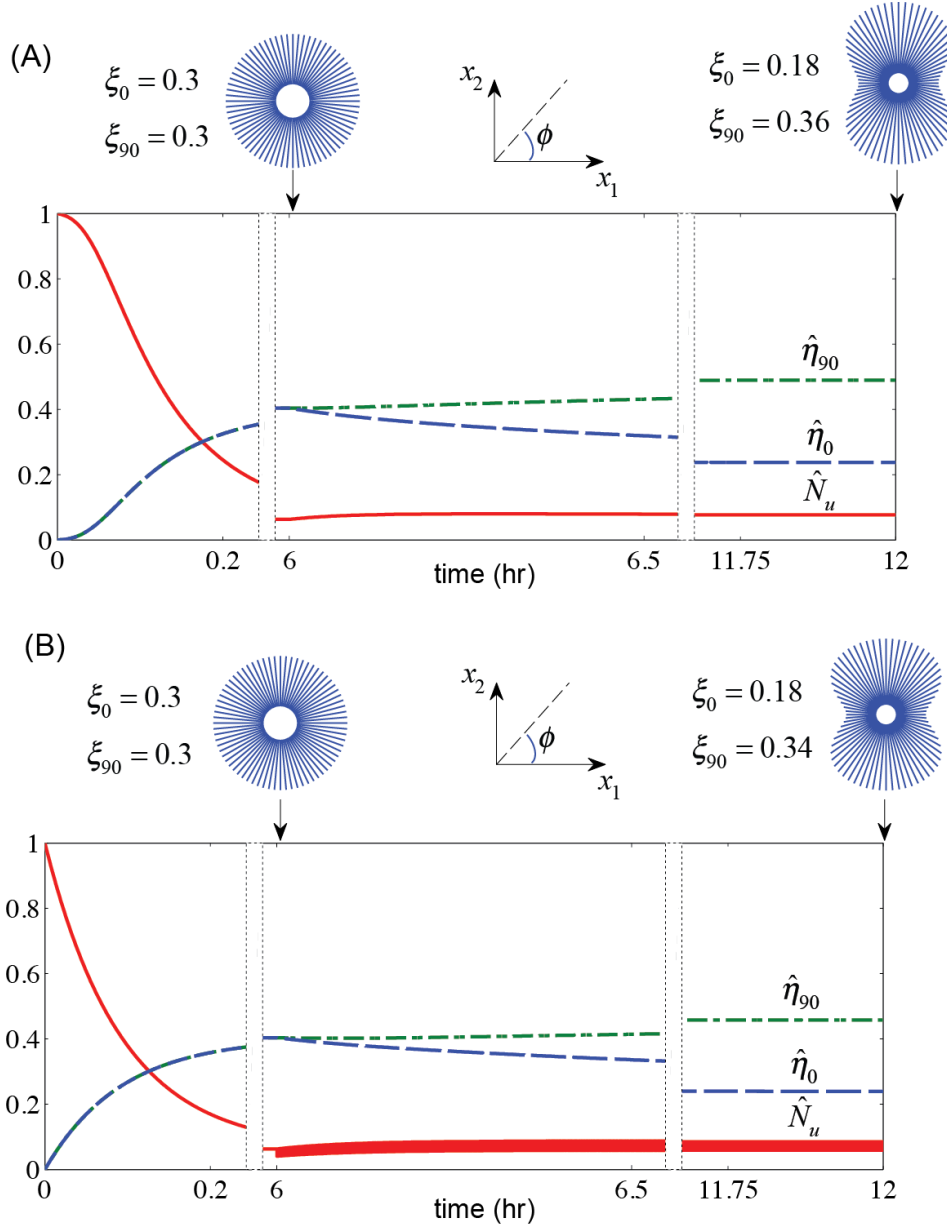


Figure 9: Predictions of the evolution of  $\hat{\eta}_{90}$ ,  $\hat{\eta}_0$  and  $\hat{N}_u$  for the (a) slow and (b) fast remodeling cases for cells on substrates (type I experiments) subjected to cyclic loading with  $E_{\max} = 0.1$  and  $f = 1$  Hz. Insets showing circular histograms of  $\xi$  at steady-state during the static and cyclic loading phases are included. The  $x$ -axis of the figures is broken into three groups so as to show the initial phase, the phase when cyclic loading is commenced and after cyclic steady-state has been attained.

*Simulations Type II experiments:* Again consistent with the cells in the Type I experiments,  $\hat{N}_T = 1$  throughout the cell with  $\hat{N}_T = 0$ . Moreover, we assume that the cells are loaded in a spatially uniform manner and thus again the boundary conditions reduce to imposing a stress and/or strain state on the cell. Recall that in these experiments the gel is constrained and cyclically stretched in one direction and free to contract in the other two orthogonal directions. Neglecting the stiffness of the gel/matrix<sup>2</sup>, we thus idealize this situation by imposing a time dependent nominal strain history  $E_{11}(t)$ ,  $E_{12} = 0$  as well as the stress-free conditions  $\Sigma_{22} = \Sigma_{33} = 0$ . Again in this 2D setting, the condition that  $\Sigma_{33} = 0$  reduces to  $\sigma_{33}^p = 0$  but the condition that  $\Sigma_{22} = 0$  implies that

<sup>2</sup> See Obbink-Huizer et al. (2014) for a detailed discussion on the effect of the gel/matrix stiffness.

$$\sigma_{22} = -\sigma_{22}^p. \quad (3.1)$$

$E_{22}(t)$  is then a solution variable that follows from the imposition of Eq. (3.1).

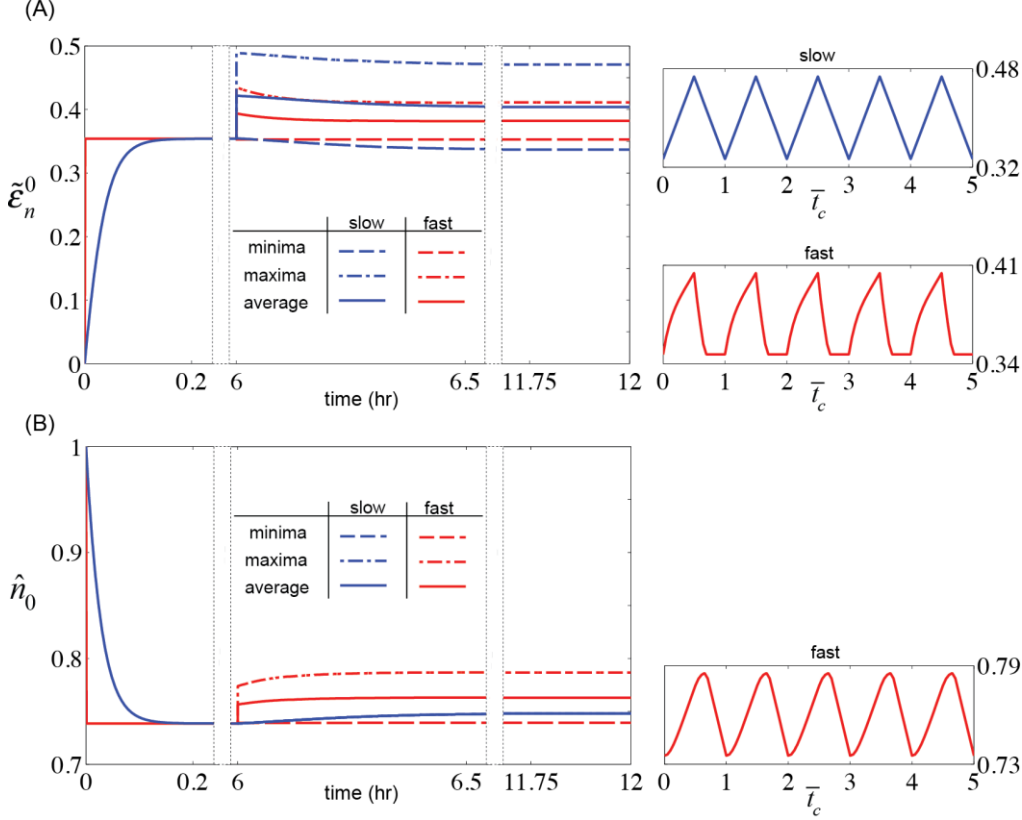


Figure 10: Predictions of the temporal evolution of (a)  $\tilde{\epsilon}_n^0$  and (b)  $\hat{n}_0$  for both the slow and fast remodeling cases for cells on substrates (type I experiments) subjected to cyclic loading with  $E_{\max} = 0.1$  and  $f = 1$  Hz. The  $x$ -axis of the figures is broken into three groups so as to show the initial phase, the phase when cyclic loading is commenced and after cyclic steady-state has been attained. Insets showing the detailed temporal variations over 5 cycles after cyclic steady-state has been attained are included in (a) for both the slow and fast cases and in (b) for only the fast case as there is negligible variation of  $\hat{n}_0$  over a cycle in the slow case.

*Initial conditions and signal:* Recall that the activation signal  $C$  is initiated by the stretching of focal adhesions on the cell membrane. Thus, we anticipate that the activation signal is re-initiated during each cycle. The period of cyclic stretching  $T \ll \zeta$ , and thus here for simplicity we assume  $C = 1$  for all times  $t \geq 0$ . It now remains to specify initial conditions for the cell. These conditions are somewhat arbitrary as the state of the cell at  $t = 0$  is difficult to quantify. Here we assume that at  $t = 0^-$  the cell is stress-fiber free with  $\hat{\eta}(\phi) = 0 \forall \phi$  and  $\hat{N}_u = 1$  and also stress free ( $\Sigma_{ij} = 0$ ). Moreover, we assume that the cell is in its ground-state with  $\epsilon_n(\phi) = 0$  and  $\hat{n}(\phi) = 1 \forall \phi$ . We emphasize that the cyclic steady-state stress-fiber distributions are not sensitive to the choice of the initial conditions.

In both the situations modeled here, the cell state is spatially uniform and there is no rigid body rotation so  $\phi = \phi^*$ . Thus, the solution of the model described in Section 2 does not involve partial differential equations but rather a set of ordinary differential equation for  $\hat{\eta}(\phi)$  and  $\hat{n}(\phi)$  in time. These were solved in commercial package MATLAB using an Euler-

Backward time integration scheme with discretization in  $\phi$  done using 36 integration points and the integration in Eq. (2.53) performed using the trapezoidal rule. While in the simulations of the type I experiments the Euler Backward solution involved solving a non-linear set of equations using a Newton-Raphson method for  $\hat{\eta}(\phi)$  and  $\hat{n}(\phi)$  the simulations of the type II experiments involved  $E_{22}$  as an additional unknown along with the associated constraint Eq. (3.1).

### 3.2 Material parameters

All simulations are reported for cells at a temperature  $T = 310$  K. Most of the parameters of the model are related to the properties of the proteins that constitute stress-fibers. These parameters are thus expected to be independent of cell type. Notable exceptions to this are: (i) the stress-fiber protein volume fraction  $f_0$  that for example is expected to be higher in smooth muscle cells compared to fibroblasts etc.; (ii) the remodeling rate constant  $\alpha$  that depends on whether the cell is for example a progenitor cell compared to a differentiated cell and (iii) the passive elastic properties. In this study, where possible, we attempt to use parameters calibrated for epithelial cells from the studies of McGarry et al. (2009) and Ronan et al. (2012) and emphasize that we anticipate only  $f_0$ ,  $\alpha$  and the passive elastic properties to change significantly with cell type. The passive elastic parameters are taken to be  $E = 5.0$  kPa and  $\nu = 0.45$ , while the maximum contractile stress  $\sigma_{\max} = 240$  kPa consistent with a wide range of measurements on muscle fibers (Lucas et al. 1995). Here we take the volume fraction  $f_0 = 0.032$  which is representative for cells such as fibroblasts with low volume fractions of stress-fibers. The critical strain-rate in the Hill relation is taken to be  $\dot{\epsilon}_0 = 0.53\text{s}^{-1}$  so that the cell retains sensitivity near the physiologically relevant frequency of 1 Hz while  $\epsilon_s = 0.3$  and  $\epsilon_p = 0.6$  (McMahon, 1984). There are no definitive data in the literature on the values of the enthalpies of the unbound and bound stress-fiber proteins and we performed a parametric study to find appropriate values of these energies. The values that were found to give good agreement with observations for a wide range of loading scenarios and taken as the reference values are  $\mu_a = 20 k_B T_0$ ,  $(\mu_{uo} + \Delta\mu_{uo}) = 8 k_B T_0$  and  $\mu_{bo} = 9 k_B T_0$ , where  $T_0 = 310$  K. The reference volume of  $n^R$  functional units is taken to be  $\Omega = 10^{-7.1} \mu\text{m}^3$  such that  $\sigma_{\max}\Omega \approx 4.4 k_B T_0$  and this retains the mechano-sensitivity of the stress-fibers. Moreover, we take  $\beta = 1.2$  with  $p = 2$  so that  $\tilde{\epsilon}_n^{ss} = 0.35$ . Thus,  $\tilde{\epsilon}_n^{ss} < \epsilon_p$  and at steady-state the isometric tension  $\sigma_0 = \sigma_{\max}$ . Since we assume  $C = 1$  throughout the loading history, the parameters  $\zeta$  and  $\Delta\mu_{uo}$  are not invoked in the calculations. Moreover, for the spatially uniform situation considered here the mobility  $\Theta$  of the unbound stress-fiber proteins does not enter the calculations and hence does not need to be specified here. Further, the spatial homogeneity implies that  $\Delta\mu_{bo}$  does not qualitatively change the results and hence cannot be calibrated based on the simulations presented here. Thus, we set  $\Delta\mu_{bo} = 0$  in the current calculations. **This choice implies that there is no direct interaction between stress-fiber in different directions, as thought to be the case for ventral stress-fibers.** Finally, we choose the rate constant  $\omega_n = 20$  Hz and present results for two values of the remodeling rate constant  $\alpha = 0.01$  Hz and 200 Hz. Subsequently, we shall refer to these as the slow and fast remodeling cases, respectively. **Actin remodeling has been shown to be significantly faster in undifferentiated cells in a stem cell line undergoing differentiation by Aref et al. (2010). Based on this, we expect that the slow remodeling case is representative of differentiated cells while the fast remodeling case is relevant to pluripotent or progenitor cells.**

### 3.3 Stress-fiber alignment characterization

The key output parameters from the model are  $\hat{\eta}(\phi, t)$ ,  $\hat{n}(\phi, t)$ ,  $\hat{N}_u$ ,  $\tilde{\epsilon}_n(\phi, t)$ ,  $\epsilon_n(\phi, t)$  and the stress state  $\Sigma_{ij}(t)$ . These direct outputs are useful in terms of developing an understanding of

the cell physics as predicted by model. However, to make comparisons with experimental data we need to devise metrics from the model that are most consistent with measurements. The experimental assessments have typically used the following procedure (Kaunas et al. 2005). A large number of experiments are conducted for each cyclic stretch condition and the cells stained with rhodamine phalloidin after a steady-state is attained (typically after 6 to 18 hrs). The rhodamine phalloidin highlights the actin within the stress-fibers and imaging of the stained cells allows for the observation of the stress-fibers. A mean value for the stress-fiber orientation is then computed for each cell by means of an image-processing algorithm based on pixel intensity gradients. Then circular histograms quantifying the number of cells observed with a particular mean stress-fiber orientation are constructed.

The output of the model presented above is not statistical and hence does not allow an identical metric to be evaluated. However, the product  $\hat{\eta}(\phi)\hat{n}(\phi)$  gives a measure of the number of functional units (and therefore actin concentration as well) at orientation  $\phi$ . Following Wei et al. (2008) (and numerous subsequent studies), we envisage that the number of cells with given mean stress-fiber orientation  $\phi$  is proportional to  $\xi \equiv \hat{\eta}(\phi)\hat{n}(\phi)$ . We then construct circular histograms with the length of individual vector components proportional to level  $\xi$  and plot these individual vectors are plotted at  $\phi$  intervals of  $5^\circ$ . This provides a direct method to compare with the circular histograms typically plotted in experimental studies.

#### 4. Comparison between cyclic loading of cells on substrates and in 3D tissues

We first consider the differences in the response of cells on substrates (type I) and constrained in 3D tissues (type II) and subject to cyclic straining. In both cases, at time  $t = 0$  the cells are constrained such that  $E_{11} = 0$  is imposed. This initial constraint is applied over the period  $0 \leq t < 6$  hr (static loading phase) and then cyclic stretch applied for  $t \geq 6$  hr for another 6 hrs (cyclic loading phase). The cells are subjected to a periodic triangular strain versus time history  $E_{11}$  that varies from 0 to  $E_{\max} = 0.1$  with a frequency  $f = 1/T = 1$  Hz. The loading and unloading rates are equal such that imposed strain-rate is  $0.2 \text{ s}^{-1}$ . For all time  $t \geq 0$ , the activation signal is assumed to be at its full level of  $C = 1$ . **It is worth emphasizing here that the initial static phase is employed to create a reasonably realistic set of initial conditions for the cyclic loading phase. We appreciate that a temporally constant signal maybe unrealistic for the initial static phase but the steady-state cyclic results are insensitive to these initial conditions and hence for simplicity we use a constant signal for all  $t \geq 0$ .**

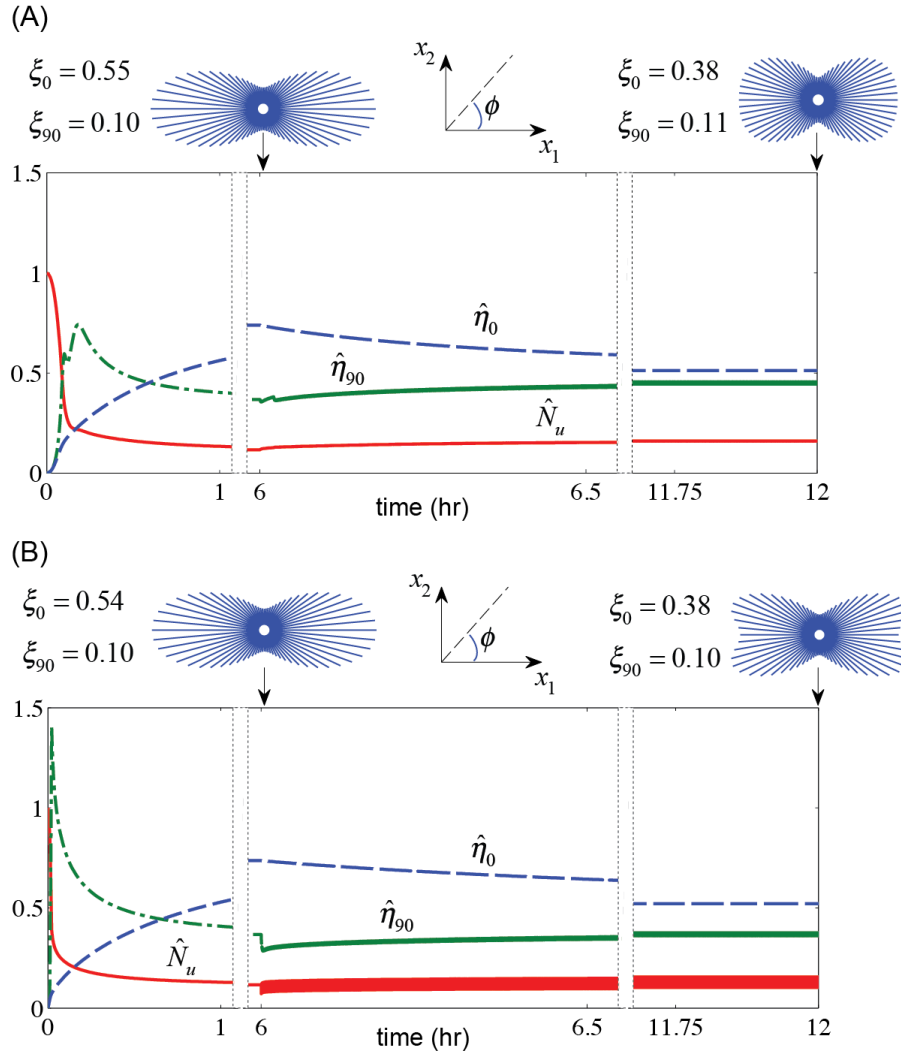


Figure 11: Predictions of the evolution of  $\hat{\eta}_{90}$ ,  $\hat{\eta}_0$  and  $\hat{N}_u$  for the (a) slow and (b) fast remodeling cases for cells constrained in 3D tissues (type II experiments) and subjected to cyclic loading with  $E_{\max} = 0.1$  and  $f = 1$  Hz. Insets showing circular histograms of  $\xi$  at steady-state during the static and cyclic loading phases are included. The  $x$ -axis of the figures is broken into three groups so as to show the initial phase, the phase when cyclic loading is commenced and after cyclic steady-state has been attained.

In order to present the results, we define  $\hat{\eta}_{90}$  and  $\hat{\eta}_0$  as the angular stress-fiber concentration  $\hat{\eta}$  in the  $\phi = 0^\circ$  and  $\phi = 90^\circ$  directions, respectively. Correspondingly,  $\hat{n}_{90}$  and  $\hat{n}_0$ ,  $\hat{\varepsilon}_n^{90}$  and  $\hat{\varepsilon}_n^0$ ,  $\varepsilon_n^{90}$  and  $\varepsilon_n^0$  and  $\xi_0$  and  $\xi_{90}$  are the non-dimensional number of functional units, nominal functional unit strains, nominal cell strains and actin concentration in the  $\phi = 0^\circ$  and  $\phi = 90^\circ$  directions, respectively.

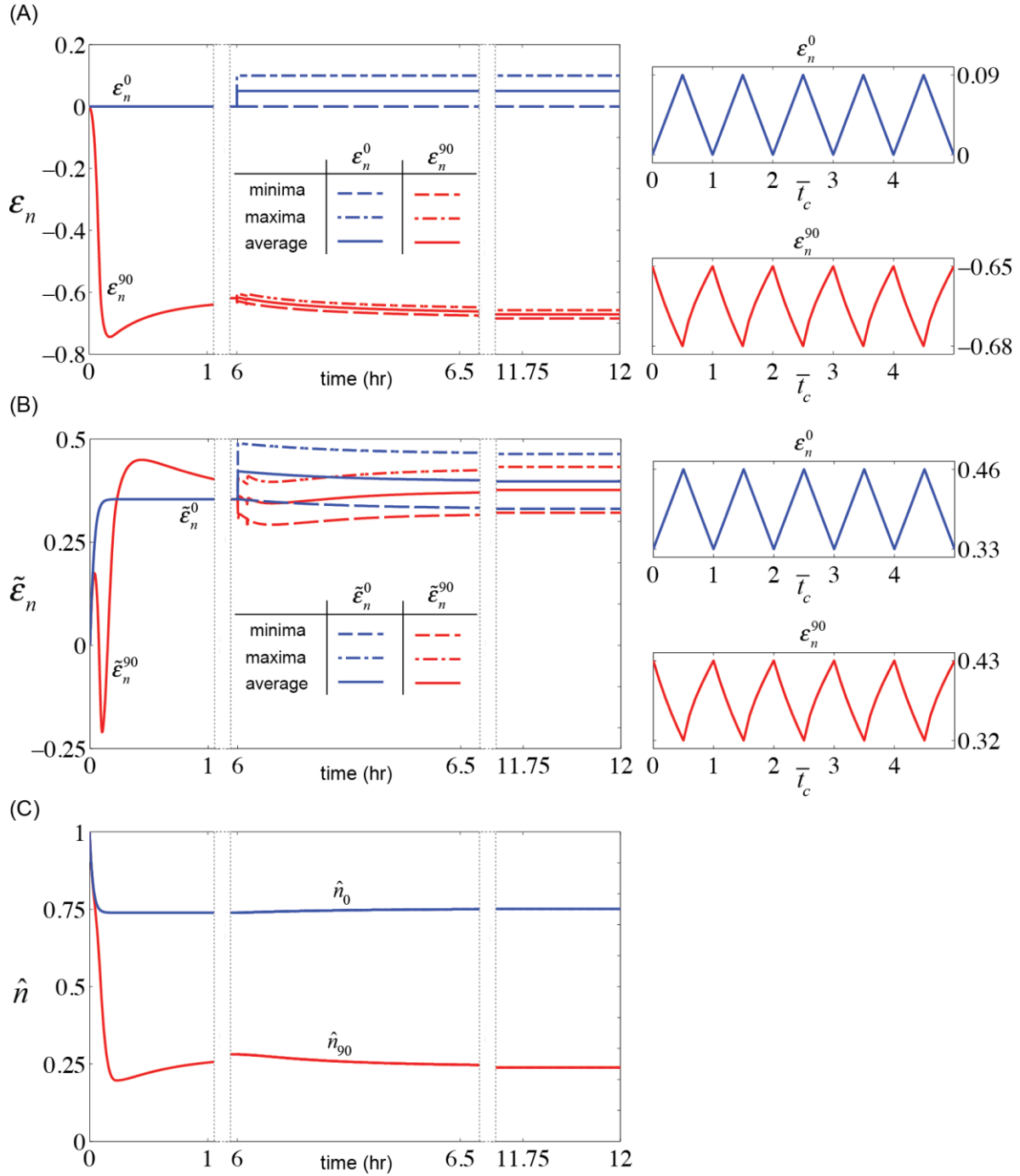


Figure 12: Predictions of the temporal evolution of (a)  $\epsilon_n^0$  and  $\epsilon_n^{90}$ , (b)  $\tilde{\epsilon}_n^0$  and  $\tilde{\epsilon}_n^{90}$  and (c)  $\hat{n}_0$  and  $\hat{n}_{90}$  for the slow remodeling case for cells constrained in 3D tissues (type II experiments) and subjected to cyclic loading with  $E_{\max} = 0.1$  and  $f = 1$  Hz. The x-axis of the figures is broken into three groups so as to show the initial phase, the phase when cyclic loading is commenced and after cyclic steady-state has been attained. In (a) and (b) we include insets showing the detailed temporal variations of  $\epsilon_n$  and  $\tilde{\epsilon}_n$  over 5 cycles after cyclic steady-state has been attained.

First consider the type I experiments. Predictions of the temporal evolution of  $\hat{\eta}_{90}$ ,  $\hat{\eta}_0$  and  $\hat{N}_u$  are included in Figs. 9a and 9b for the slow and fast remodeling cases, respectively. At the initiation of the signal at  $t = 0$ , stress-fiber concentrations  $\hat{\eta}_{90}$  and  $\hat{\eta}_0$  begin to increase (and consequently  $\hat{N}_u$  decreases) rapidly. With both  $E_{11} = E_{22} = 0$ , the stress-fibers grow in an isotropic manner and thus over the time period  $0 \leq t \leq 6$  hr and the curves of  $\eta_{90}$  and  $\eta_0$  are

indistinguishable in Figs. 9a and 9b. Insets of the circular histograms of  $\xi$  are included in Figs. 9a and 9b at the end of the static loading phase at  $t = 6$  hr and confirm that actin distribution is isotropic as well. While the temporal evolution of  $\hat{\eta}$  is nearly identical for both the fast and slow remodeling cases, the evolution of  $\hat{n}$  and  $\tilde{\varepsilon}_n$  is significantly different in the two cases. We include the temporal evolutions of  $\tilde{\varepsilon}_n^0$  in Fig. 10a and  $\hat{n}_0$  in Fig. 10b for both the slow and fast remodeling cases. For the static loading at times  $t \leq 6$  hr,  $\tilde{\varepsilon}_n$  and  $\hat{n}$  are equal in all directions and reach their steady-state values of  $\tilde{\varepsilon}_n^{SS}$  and  $\hat{n}^{SS}$  almost instantaneously for cells undergoing fast remodeling. On the other hand, it takes about 500 s for the cells undergoing slow remodeling to reach these steady-state values.

Now consider the cyclic loading of these cells which commences at  $t = 6$  hr. In both the fast and slow remodeling cases,  $\hat{\eta}_{90}$  increases while  $\hat{\eta}_0$  decreases and there is a negligible change to  $\hat{N}_u$  (Fig. 9). The final steady-state distributions of the actin concentrations as parameterized by  $\xi$  are included as circular histograms in insets of Fig. 9. Clearly, the actin distributions are now anisotropic and, consistent with observations (e.g. Kaunas et al. 2005), the model predicts that stress-fibers form primarily in the direction perpendicular to the direction of cyclic straining. To understand this recall that the stress-fiber stress drops as per the Hill-like relation (2.36) during the unloading phase  $\dot{E}_{11} < 0$  which increases the enthalpies of the stress-fibers around the  $\phi = 0^\circ$  direction and thus preferentially increases the dissociation of these stress-fibers. By contrast, stress-fibers around the  $\phi = 90^\circ$  direction are subjected to relatively small strain-rates even during the cyclic loading phase and thus do not undergo enhanced dissociation.

The temporal evolution of  $\tilde{\varepsilon}_n^0$  is included Fig. 10a for the last 5 cycles of loading and the corresponding variation of  $\hat{n}_0$  plotted in Fig. 10b. These detailed evolutions are plotted in insets in Fig. 10 using the axis  $\bar{t}_c \equiv ft_c$ , where time  $t_c = 0$  corresponds to the start of the first of the first of the 5 cycles plotted. For cells undergoing fast remodeling,  $\tilde{\varepsilon}_n^0$  increases in a nonlinear manner during the stretching phase of the loading but decreases rapidly (and linearly) back to  $\tilde{\varepsilon}_n^{SS}$  and then remains at this value during the remainder of the unloading phase of the cyclic loading. To understand this asymmetry recall that  $\hat{n}$  is proportional to  $\hat{N}_u$  when functional units are being added to a stress-fiber. With  $\hat{N}_u \rightarrow 0$ , the rate  $\dot{\hat{n}}$  is limited by the availability of unbound functional units during the stretching phase and hence  $\dot{\hat{n}}$  is relatively slow. On the other hand, during unloading, functional units are being dissociated from stress-fibers and this process is very rapid. In the slow remodeling cases, nearly no addition or dissociation of functional units takes place over the period of a single cycle and hence  $\dot{\hat{n}}_0 \approx 0$  and consequently  $\dot{\tilde{\varepsilon}}_n^0 \approx \dot{\varepsilon}_n^0$  i.e.  $\tilde{\varepsilon}_n^0$  has the same imposed triangular form as  $E_{11}$ .

Next consider the type II experiments. The time evolution of  $\hat{\eta}_{90}$  and  $\hat{\eta}_0$  as well as  $\hat{N}_u$  are included in Figs. 11a and 11b for the slow and fast remodeling cases, respectively. Very early in the initial static phase,  $\hat{\eta}_{90}$  rises rapidly and then starts to decay while  $\hat{\eta}_0$  increases monotonically from its initial value of zero. At the steady-state during the static loading phase  $\hat{\eta}_0 > \hat{\eta}_{90}$  and the corresponding circular histogram of the non-dimensional actin concentration  $\xi$  is included as insets in Fig. 11. Unlike in the type I experiments, a strongly anisotropic distribution is observed with a high concentration of both stress-fibers and the actin concentration around the  $\phi = 0^\circ$  direction. To rationalize these results consider the corresponding variations of  $\varepsilon_n^0$  and  $\varepsilon_n^{90}$  in Fig. 12a,  $\tilde{\varepsilon}_n^0$  and  $\tilde{\varepsilon}_n^{90}$  in Fig. 12b and  $\hat{n}_0$  and  $\hat{n}_{90}$  in Fig. 12c for the slow remodeling case. Early in the loading history  $\varepsilon_n^{90}$  reduces as stress-fibers start to form and contract the cell in the  $x_2$ - direction (recall that  $\Sigma_{22} = 0$ ). This results in increase in the enthalpy of the fibers in the  $\phi = 90^\circ$  direction compared to those in the

$\phi = 0^\circ$  direction. Thus, stress-fibers in the  $\phi = 0^\circ$  direction are more stable and with increasing time  $\hat{\eta}_0$  continues to increase with the functional units to form these fibers resulting from the dissociation of fibers around the  $\phi = 90^\circ$  direction. Importantly, at steady-state during the static loading phase  $\tilde{\varepsilon}_n^0 = \tilde{\varepsilon}_n^{90} = \tilde{\varepsilon}_n^{SS}$  and thus the stress-fibers which are under isometric conditions in all directions are under a tensile stress  $\sigma_0 = \sigma_{\max}$ . The above arguments are also true for the fast remodeling case, albeit the time-scales are shorter and hence curves corresponding to Fig. 12 for the fast remodeling case are omitted for the sake of brevity.

Now consider the cyclic loading phase in these type II experiments. Cyclic strain in the  $x_1 -$  direction results in a reduction in  $\hat{\eta}_0$ , in a small increase in  $\hat{\eta}_{90}$  (Fig. 11) and negligible changes in  $\hat{n}_{90}$  and  $\hat{n}_0$  (Fig. 12). The reduction in  $\hat{\eta}_0$  due to the fact that the stress-fiber stress drops as per the Hill-like relation during the  $\dot{E}_{11} < 0$  phase which increases the enthalpy of the stress-fibers around the  $\phi = 0^\circ$  direction relative to those around the  $\phi = 90^\circ$  direction. However, the imposed cyclic strain levels are relatively small and do not appreciably affect the number of functional units within the stress-fibers as seen in Fig. 12. Circular histograms of  $\xi$  at steady-state during the cyclic loading phase are included as insets in Fig. 11. While there is some reduction in the level of anisotropy compared to the steady-state during the static loading phase, it is clear that unlike in the type I experiments stress-fibers and actin concentrations are higher in the direction of the imposed loading consistent with a range of experimental observations; see for example Neiponice et al. (2007). It is worth emphasizing here that even under cyclic steady-state conditions the stress-fibers in the  $\phi = 90^\circ$  direction are under isometric conditions with functional unit strain  $\tilde{\varepsilon}_n^{90} = \tilde{\varepsilon}_n^{SS}$  and thus generate a tensile stress  $\sigma_0 = \sigma_{\max}$ . **Therefore, the reason for these stress-fibers to be less stable compared to those around the  $\phi = 0^\circ$  direction (i.e.  $\hat{\eta}_{90} < \hat{\eta}_0$ ) is that  $\hat{n}_{90} < \hat{n}_0$ .**

The model thus accurately predicts the apparently contradictory observations in the type I and type II experiments. The key to the difference is that in the type I experiments straining is prevented in the direction perpendicular ( $\phi = 90^\circ$  direction) to the imposed cyclic strain. Thus, the length of the stress-fibers in both directions are approximately equal. However, the negative strain-rate imposed in the  $\phi = 0^\circ$  direction during the shortening phase increases the enthalpy of the stress-fibers in the  $\phi = 0^\circ$  direction relative to the  $\phi = 90^\circ$  direction. This results in stress-fibers preferentially forming perpendicular to the imposed cyclic strain. By contrast, in the type II experiments the cell contracts significantly in the  $\phi = 90^\circ$  direction. This implies that these fibers have fewer functional units compared to the fibers in the  $\phi = 0^\circ$  direction. This decreases the stability of the fibers in the  $\phi = 90^\circ$  direction relative to the  $\phi = 0^\circ$  direction. The increase in the enthalpy of the stress-fibers in the  $\phi = 0^\circ$  direction during the  $\dot{E}_{11} < 0$  phase of the cyclic loading is relatively small compared to the difference in the enthalpies due to the differences in the number of functional units. Thus, in the type II experiments stress-fibers preferentially form in the direction of the imposed cyclic strain.

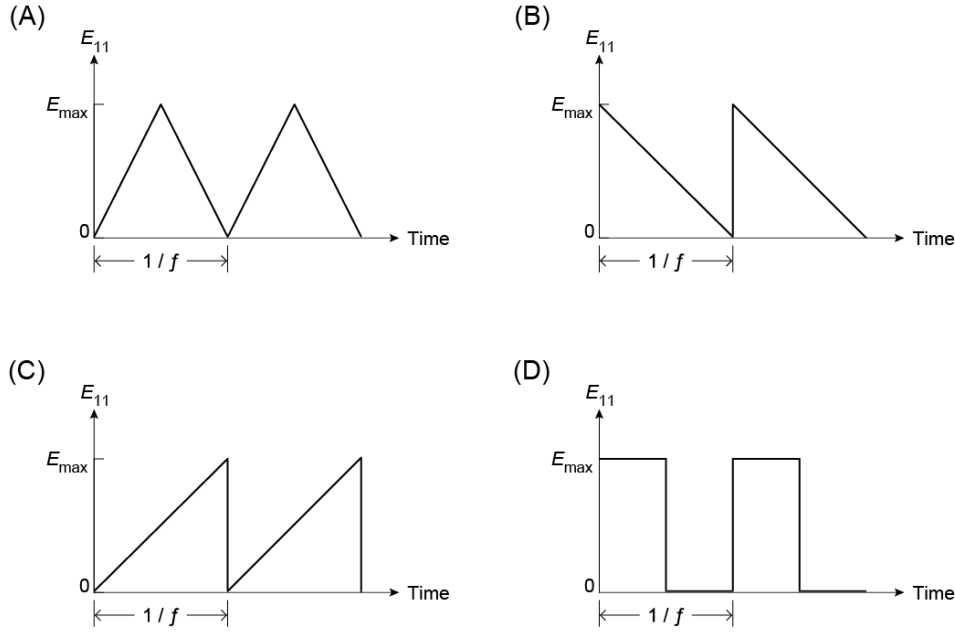


Figure 13: Sketches showing the different waveforms employed to investigate the response of cells on substrates (type I experiments) subjected to cyclic loading with  $E_{\max} = 0.1$  and  $f = 0.1$  Hz. (a) Symmetric triangular waveform; (b) triangular waveform with fast lengthening; (c) triangular waveform with fast shortening and (d) square waveform.

## 5. Dependence of response of cells on substrates (Type I) on the cyclic waveform

There are a range of experimental observations which demonstrate the strong dependence of the response of cells on substrates to the precise nature of the cyclic loading. While a range models have been developed to rationalize some of these observations here we demonstrate that the model developed in Section 2 predicts all these sometimes apparently contradictory observations in a single framework. In all simulations presented subsequently, the cells are first allowed to reach a static steady-state by imposing  $E_{ij} = 0$  over the time period  $0 \leq t \leq 6$  hr and cyclic straining is then imposed for a further 6 hrs.

### 5.1 Effect of the shape of the cyclic waveform

Tondon et al. (2012) demonstrated a strong dependence on the shape of the cyclic waveform on the response of U2OS osteosarcoma cells cultured on substrates. In particular they considered four imposed strain waveforms as sketched in Fig. 13. In all cases, the frequency of loading was  $f = 0.1$  Hz and the imposed strain varied between 0 and  $E_{\max} = 0.1$ . When the imposed strain waveform was triangular with equal loading and unloading rates (Fig. 13a), the cells did not show any sensitivity to the loading with the stress-fibers arranging randomly. However, with a fast lengthening rate and slow shortening rate, (Fig. 13b) the stress-fibers aligned perpendicular to the straining direction and this behavior was also present for the square imposed strain versus time history (Fig. 13d). However, similar to the symmetric triangular imposed strain history, when the cells were subjected to a waveform with a slow lengthening rate but fast shortening rate (Fig. 13c), the cells again did not show any sensitivity to the imposed loading with the stress-fibers arranging randomly. We attempt to explain these observations using the model developed in Section 2.

The U2OS osteosarcoma cells were originally derived from a moderately differentiated sarcoma of the tibia and thus we expect the fast remodeling limit to be more appropriate for

these cells. Hence we first consider this limit. A summary of the predictions of the model for the four different imposed strain waveforms is shown in Fig. 14 and includes (i) circular histograms of  $\xi$  at steady-state after cyclic loading; (ii) the variation of  $\tilde{\varepsilon}_n^0$  and  $\tilde{\varepsilon}_n^{90}$  with time over 5 cycles during the steady-state phase and (iii) the corresponding variations of  $\hat{n}_0$  and  $\hat{n}_{90}$ . In all cases,  $\dot{\tilde{\varepsilon}}_n^{90} = \dot{\hat{n}}_{90} = 0$  as the imposed strain-rate in the  $\phi = 90^\circ$  direction is zero and thus the state of the stress-fibers at cyclic steady-state does not vary over the period of a cycle.

For the imposed symmetric triangular waveform (Fig. 13a), the distribution of  $\xi$  (Fig. 14a) is seen to be approximately isotropic, consistent with the experimental observations. This is due to the fact that the relatively slow imposed strain-rate allows for the stress-fiber to remodel at a rate approximately equal to the imposed strain-rate and thus  $\dot{\tilde{\varepsilon}}_n^0 \approx 0$  (Fig. 14) with  $\tilde{\varepsilon}_n^0 \approx \hat{n}_0$ , i.e. the stress-fiber strain-rate in the  $\phi = 0^\circ$  fibers is approximately zero even though the cell is subjected to a non-zero strain-rate  $\dot{\varepsilon}_n^0$ . Since the stress-fiber strain-rate is approximately zero in all directions, the cells display no sensitivity to the imposed cyclic loading, i.e.  $\xi$  distribution remain is isotropic.

Now consider the case of fast lengthening (Fig. 13b). We model this by imposing an instantaneous lengthening from  $E_{11} = 0$  to  $E_{11} = E_{\max}$  followed by shortening at a rate  $\dot{E}_{11} = -fE_{\max}$ . Now, consistent with the experimental observations, the distribution of  $\xi$  at steady-state is strongly anisotropic with alignment predicted perpendicular to the direction of imposed loading. To understand this now recall that the fast lengthening implies that the stress-fibers now cannot remodel at a rate equal to the imposed loading and thus  $\tilde{\varepsilon}_n^0$  increases rapidly over the lengthening phase of the loading (Fig. 14b). Then during the relatively slow shortening phase,  $\tilde{\varepsilon}_n^0$  decreases back to its steady-state value of  $\tilde{\varepsilon}_n^{SS}$  and thus the stress-fibers now are subjected to a large negative strain-rate over a time period on the order of  $1/\alpha$ . The stress-fiber stress decreases in this period as per the Hill-like relation which in turn increases the enthalpy of these fibers and thereby increases their dissociation rate. No such dissociation takes place in the  $\phi = 90^\circ$  direction and this results in the anisotropic  $\xi$  distribution with an alignment perpendicular to the imposed loading.

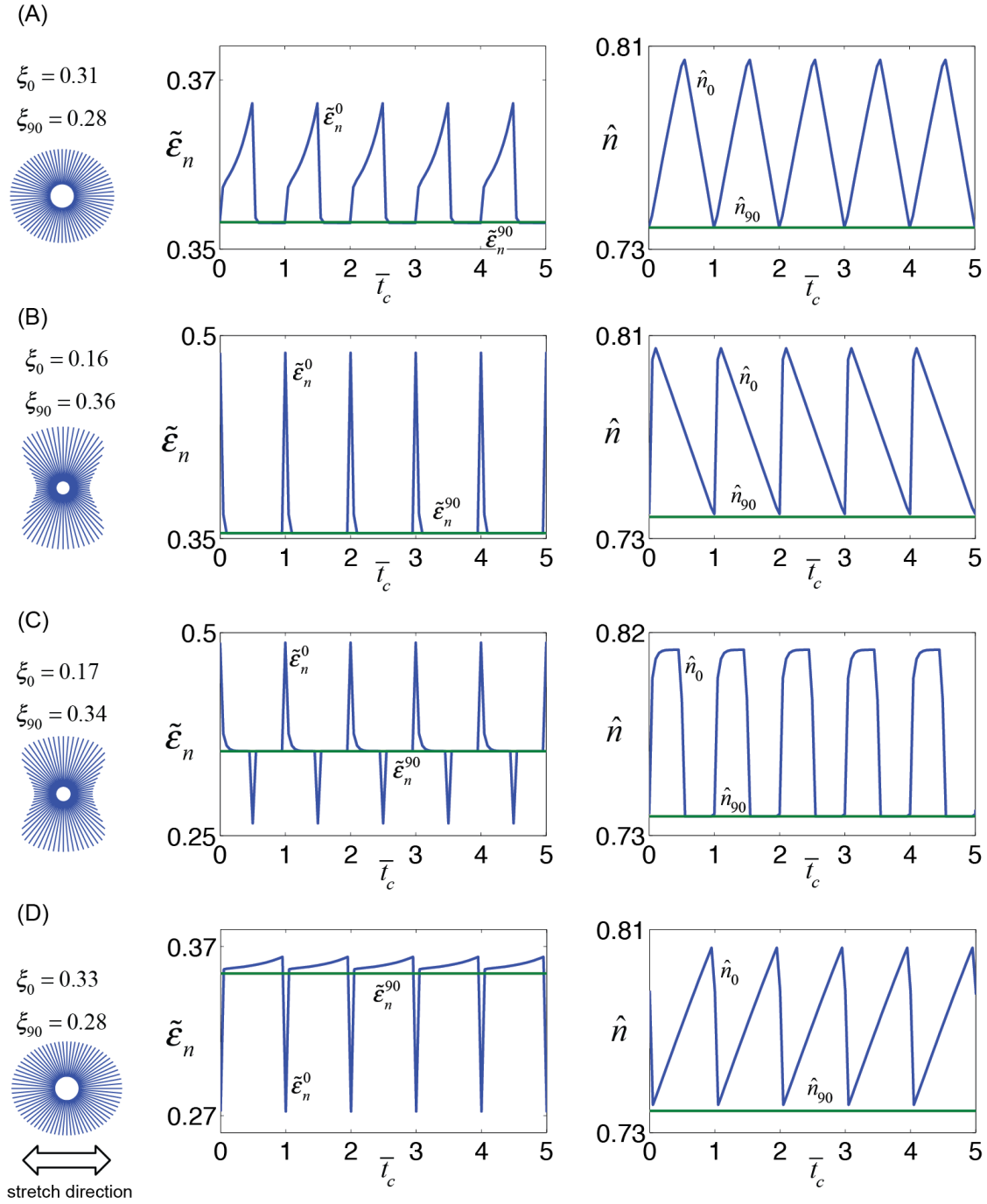


Figure 14: Predictions of the response of cells (fast stress-fiber remodeling) on substrates (type I experiments) subjected to cyclic loading with (a) symmetric triangular, (b) fast lengthening, (c) square and (d) fast shortening waveforms and  $E_{\max} = 0.1$  and  $f = 0.1$  Hz. Results are shown for (i) circular histograms of  $\xi$  at steady-state after cyclic loading; (ii) the variation of  $\tilde{\epsilon}_n^0$  and  $\tilde{\epsilon}_n^{90}$  with time over 5 cycles during the steady-state phase and (iii) the corresponding variations of  $\hat{n}_0$  and  $\hat{n}_{90}$ .

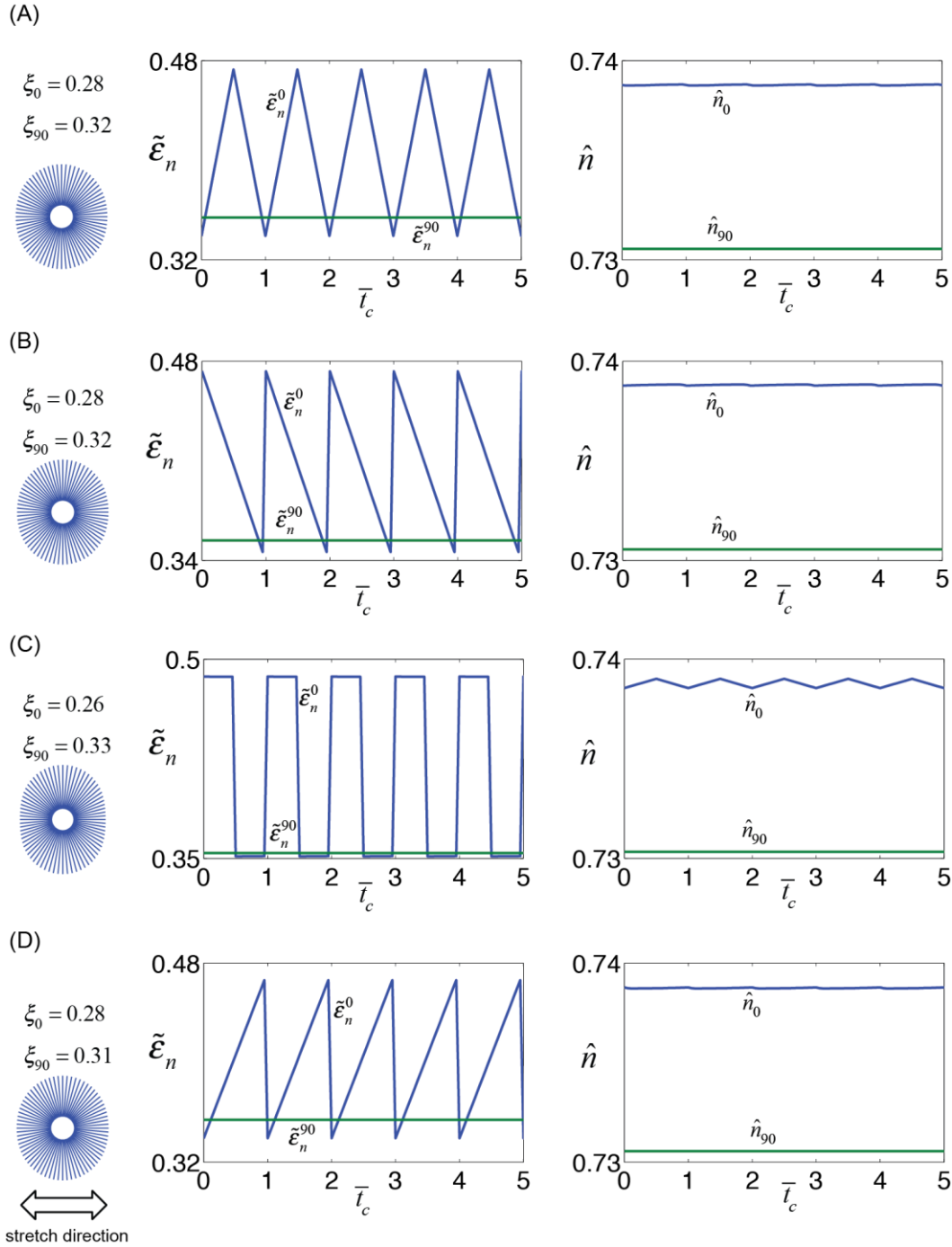


Figure 15: Predictions of the response of cells (slow stress-fiber remodeling) on substrates (type I experiments) subjected to cyclic loading with (a) symmetric triangular, (b) fast lengthening, (c) square and (d) fast shortening waveforms and  $E_{\max} = 0.1$  and  $f = 0.1$  Hz. Results are shown for (i) circular histograms of  $\xi$  at steady-state after cyclic loading; (ii) the variation of  $\tilde{\epsilon}_n^0$  and  $\tilde{\epsilon}_n^{90}$  with time over 5 cycles during the steady-state phase and (iii) the corresponding variations of  $\hat{n}_0$  and  $\hat{n}_{90}$ .

We now impose a square strain waveform by imposing an instantaneous lengthening from  $E_{11} = 0$  to  $E_{11} = E_{\max}$  then  $\dot{E}_{11} = 0$  for a time period  $1/(2f)$  and then instantaneously decreasing the strain from  $E_{11} = E_{\max}$  to  $E_{11} = 0$  again followed by  $\dot{E}_{11} = 0$  for a time period  $1/(2f)$ . Similar to the fast lengthening case, the stress-fibers around the  $\phi = 0^\circ$  direction are subjected to a large negative strain-rate in the period immediately after the imposed lengthening which results in their dissociation. However, in addition in this case

they are also subjected to a large lengthening rate following the imposed shortening. This lengthening does not result in any significant change to their enthalpy as the in the Hill-like relative we assume that the stress-fiber stress remains at its isometric value for positive strain-rates. Thus, again similar to the fast lengthening (and consistent with experimental observations) a  $\xi$  distribution aligned perpendicular to the imposed loading direction is predicted (Fig. 14c) due to dissociation of stress-fibers around the  $\phi = 0^\circ$  direction immediately after the lengthening phase of the imposed loading.

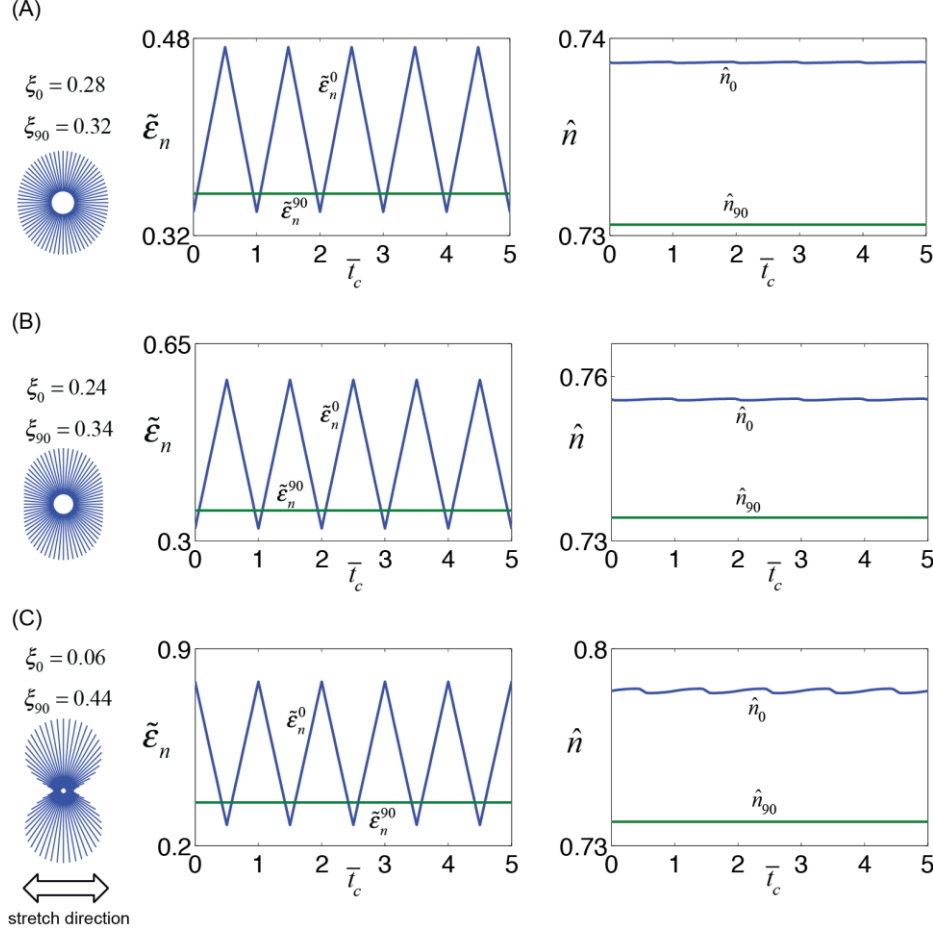


Figure 16: Predictions of the response of cells (slow stress-fiber remodeling) on substrates (type I experiments) subjected to cyclic loading with symmetric triangular waveform and strain-rate  $|\dot{E}_{11}| = 0.02 \text{ s}^{-1}$  for strain amplitudes (a)  $E_{\max} = 0.1$ , (b) 0.2 and (c) 0.4. Results are shown for (i) circular histograms of  $\xi$  at steady-state after cyclic loading; (ii) the variation of  $\tilde{\epsilon}_n^0$  and  $\tilde{\epsilon}_n^{90}$  with time over 5 cycles during the steady-state phase and (iii) the corresponding variations of  $\hat{n}_0$  and  $\hat{n}_{90}$ .

Finally consider the case of fast shortening (Fig. 13c). Here as seen in Fig. 14d, we predict negligible sensitivity to the imposed loading consistent with the experimental observations. This is rationalized by noting that now the stress-fibers around the  $\phi = 0^\circ$  direction are subjected to a large positive strain-rate over a finite time period following the imposed instantaneous shortening. This does not affect the enthalpy of these stress-fibers and hence their dissociation rate is not affected. This results in the insensitivity of the cells to this type of imposed cyclic loading and the predicted isotropic distribution of  $\xi$ . **We note in passing that we have also conducted simulations at a frequency  $f = 0.01 \text{ Hz}$  and confirmed that, consistent with the results of Tondon et al. (2012) for the symmetric and fast shortening cases, the stress-fiber alignment was near perfectly isotropic while strong alignment**

perpendicular to the direction of straining was predicted in the other two cases.

The corresponding predictions for the slow remodeling case are summarized in Fig. 15. Now, unlike the observations of Tondon et al. (2012), the model predicts negligible sensitivity of the cells to all the four cases of the imposed loading<sup>3</sup>. To understand this recall that the sensitivity of the cells in the fast remodeling case resulted from the negative strain-rates that the stress-fibers around the  $\phi = 0^\circ$  direction were subjected to over a time period of  $1/\alpha$  following the fast lengthening. However, in the slow remodeling case the stress-fibers remodel over a period significantly longer than the imposed cyclic loading period  $1/f$  and thus the stress-fibers  $\phi = 0^\circ$  direction are always subjected to strain-rate  $\dot{\xi}_n^0 \approx \dot{\xi}_n^0$ . With  $\dot{\xi}_n^0 \ll \dot{\xi}_0$ , the stress-fibers are near isometric conditions for all the loading histories imposed here and hence the cells in the slow remodeling case display negligible sensitivity to the imposed cyclic loading. We thus predict that differentiated cells (for which the slow remodeling limit is most applicable) will not display the sensitivities observed by Tondon et al. (2012): this prediction requires experimental verification.

### 5.2 Effect of strain amplitude

The studies of Kaunas et al. (2005) and Jungbauer et al. (2008) have demonstrated that the propensity of stress-fibers to align perpendicular to the loading direction increases with increasing applied strain-rate for a triangular imposed strain waveform. For example, as seen above with a strain amplitude of 0.1, the stress-fibers align perpendicular to the imposed loading direction when the cyclic frequency  $f = 1$  Hz but the stress-fiber distribution is approximately isotropic when  $f = 0.1$  Hz. Equally if the frequency was fixed at  $f = 1$  Hz and the strain amplitude decreased from 0.1 to 0.01 (Kaunas et al. 2005), the model predicts that, consistent with observations the alignment of stress-fibers reduces (not shown here for the sake of brevity). This suggests that with decreasing imposed strain-rate the sensitivity of cells to cyclic loading decreases. However, Faust et al. (2011) demonstrated that for umbilical cord fibroblasts subjected to cyclic straining at low frequencies (on the order of mHz), the stress-fibers reorient in a direction perpendicular to the imposed loading when the applied strain amplitude exceeds a critical value. This suggests these fibroblasts develop sensitivity to cyclic loading at large applied strain amplitudes even at applied strain-rates  $\ll \dot{\xi}_0$ . We now proceed to present results for symmetric triangular imposed strain histories with the loading/unloading strain-rate magnitude kept fixed at  $|\dot{E}_{11}| = 0.02 \text{ s}^{-1}$  and the cells strained from  $E_{11} = 0$  to  $E_{11} = E_{\max}$  and the amplitude  $E_{\max}$  varied.

Umbilical cord fibroblasts are differentiated cells and hence the slow remodeling limit is more applicable to these cells. We thus first present results for the slow remodeling limit. The predictions of the model are summarized in Fig. 16 for three values of  $E_{\max} = 0.1, 0.2$  and  $0.4$  corresponding to cyclic frequencies  $f = 0.1$  Hz,  $0.05$  Hz and  $0.025$  Hz, respectively. In Fig. 16 (similar to Figs. 14 and 15) we show the predictions of the circular histograms of  $\xi$  at cyclic steady-state and the variation of  $\dot{\xi}_n^0$  and  $\dot{\xi}_n^{90}$  with time over 5 cycles during the cyclic steady-state phase and the corresponding variations of  $\hat{n}_0$  and  $\hat{n}_{90}$ . Again, since imposed strain-rates are zero in the  $\phi = 90^\circ$  direction there is no variation of  $\dot{\xi}_n^{90}$  and  $\hat{n}_{90}$  at steady-state. Consistent with the observations of Faust et al. (2011), the model predicts isotropic stress-fiber distributions when  $E_{\max} = 0.1$  but the distribution of  $\xi$  becomes more anisotropic

---

<sup>3</sup> A mildly anisotropic distribution of  $\xi$  with alignment perpendicular to the imposed loading for the fast lengthening and square waveform cases.

with increasing  $E_{\max}$  with a clear alignment of stress-fibers perpendicular to the loading direction predicted in the  $E_{\max} = 0.4$  case. To understand this strain dependence at these very slow imposed cyclic frequencies, let us consider the  $E_{\max} = 0.4$  case corresponding to  $f = 0.025$  Hz, i.e. a cyclic period of 40 s. Remodeling of the stress-fibers occurs on the time-scale of about  $1/\alpha = 100$  s and thus even at their very low imposed loading frequencies  $\dot{\xi}_n^0 \approx \dot{\xi}_n^0$  and  $\hat{n}_0 \approx 0$  as seen in Fig. 16. Thus, the stress-fibers in all directions are near isometric conditions as  $|\dot{E}_{11}| \ll \dot{\xi}_0$ . However, the large imposed strain amplitudes now implies that  $\tilde{\xi}_n^0$  now exceeds  $\varepsilon_p + \varepsilon_s$ . Thus, via Eq. (2.37) the isometric stress  $\sigma_0$  reduces significantly and consequently the stress-fiber stress also reduces even though the imposed strain-rates are small. This reduction in the stress-fiber stress increases the enthalpy of the stress-fibers and consequently the dissociation rate of fibers around the  $\phi = 0^\circ$  direction. Stress-fibers around the  $\phi = 90^\circ$  direction are not subjected to large strains and hence remain relatively unaffected. This preferential dissociation of stress-fibers around the  $\phi = 0^\circ$  direction results in the anisotropic distribution of  $\xi$  with stress-fibers aligned perpendicular to the loading direction. This behavior at low applied frequencies only occurs when the stress-fiber strains exceed  $\varepsilon_p$  and this gives rise to the critical strain amplitude observed by Faust et al. (2011) above which cells have a sensitivity to cyclic loading at low frequencies.

Now consider the fast remodeling case. We again consider the same three cases presented in Fig. 16 but add an additional (albeit unrealistic) loading case of  $E_{\max} = 1.0$  corresponding to  $f = 0.01$  Hz. The predictions of the model are summarized in Fig. 17 in the manner analogous to Figs. 14-16. Consistent with observations, an isotropic distribution of  $\xi$  is predicted in the  $E_{\max} = 0.1$  case. However, for  $E_{\max} = 0.2$  and  $0.4$  the stress-fibers are predicted to preferentially align *with* the loading direction although this alignment is relatively weak at-least in the  $E_{\max} = 0.2$  case. In order to understand this behavior, consider the  $\tilde{\xi}_n^0$  history for the  $E_{\max} = 0.4$  case shown in Fig. 17. Recall that we anticipate remodeling to take place on a time-scale on the order of  $1/\alpha = 5$  ms, i.e. much faster compared to the imposed cyclic loading period and thus we would anticipate  $\dot{\xi}_n^0 \approx 0$ . However, remodeling on this time scale can only occur if functional units are available for remodeling. We include in Fig. 18a the predictions of the temporal evolution of  $\hat{\eta}_0$ ,  $\hat{\eta}_{90}$  and  $\hat{N}_u$  for this  $E_{\max} = 0.4$  case over the 5 cycles corresponding to the results in Fig. 17. It is clear that  $\hat{N}_u \rightarrow 0$  over the stretching phase of the loading. This implies that even though the stress-fibers  $\phi = 0^\circ$  direction are being stretched and addition of functional units would reduce their enthalpy no functional units are available for this purpose. This results in an increase in  $\tilde{\xi}_n^0$  during the stretching phase but  $\tilde{\xi}_n^0$  drops rapidly back to its steady-state value of  $\tilde{\xi}_n^{SS}$  during the unloading phase when functional units can readily dissociate from the stress-fibers and result in an increase in  $\hat{N}_u$ . Thus, during the stretching phase  $\tilde{\xi}_n^0$  reaches a maximum value of approximately 0.54. While this is greater than  $\varepsilon_p$  it is less than  $\varepsilon_p + \varepsilon_s$  and therefore the stress-fiber stress does not drop significantly and the resulting increase in the enthalpy of the stress-fibers around the  $\phi = 0^\circ$  direction is small. However, a consequence of the significant growth in length of the stress-fibers around the  $\phi = 0^\circ$  direction is that  $\hat{n}_0$  increases significantly as seen in Fig. 17. This increase in the number of functional units in the stress-fibers stabilizes the stress-fibers around the  $\phi = 0^\circ$  direction due to an increase in  $\hat{n}(\mu_T - \mu_b)$  and reduces their dissociation rate relative to the fibers around the  $\phi = 90^\circ$  direction. Therefore, the distribution of  $\xi$  is anisotropic in this  $E_{\max} = 0.4$  case with stress-fibers predicted to preferentially align with the loading direction.

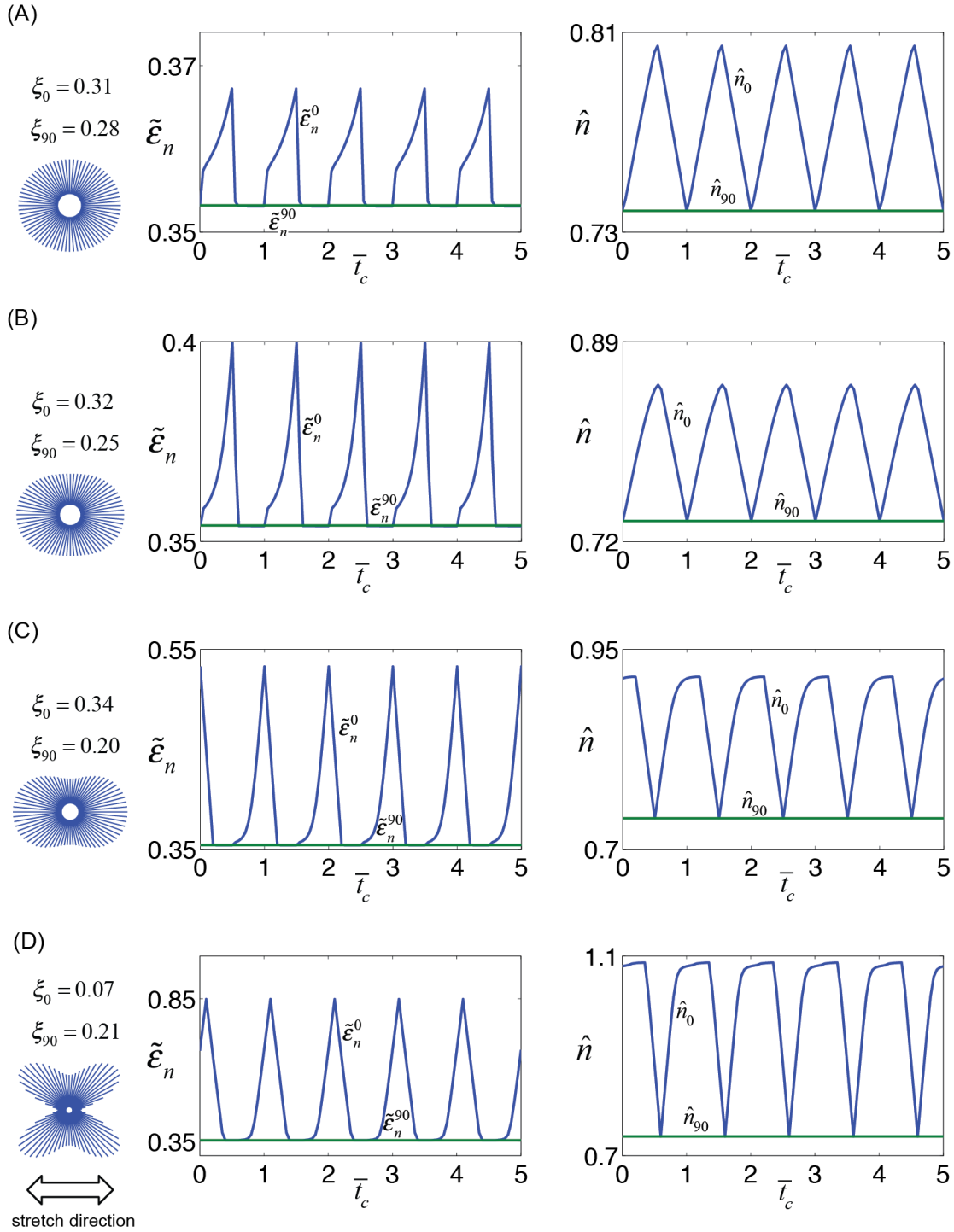


Figure 17: Predictions of the response of cells (fast stress-fiber remodeling) on substrates (type I experiments) subjected to cyclic loading with symmetric triangular and strain-rate  $|\dot{E}_{11}| = 0.02 \text{ s}^{-1}$  for strain amplitudes (a)  $E_{\max} = 0.1$ , (b)  $E_{\max} = 0.2$ , (c)  $E_{\max} = 0.4$  and (d)  $E_{\max} = 1.0$ . Results are shown for (i) circular histograms of  $\xi$  at steady-state after cyclic loading; (ii) the variation of  $\tilde{\epsilon}_n^0$  and  $\tilde{\epsilon}_n^{90}$  with time over 5 cycles during the steady-state phase and (iii) the corresponding variations of  $\hat{n}_0$  and  $\hat{n}_{90}$ .

Now consider the extreme case of  $E_{\max} = 1.0$  with fast remodeling of the stress-fibers. The distribution of  $\xi$  at cyclic steady-state is now predicted to have a “butterfly” shape with a low stress-fiber concentration in both the  $\phi = 0^\circ$  and  $90^\circ$  directions with  $\xi$  maximum at  $\phi \approx$

$\pm 45^\circ$ . To rationalize, recall that stretching of the cell to large strains results in the cell running out of functional units to remodel the stress-fibers. This effect is now very significant as seen in the plot of  $\hat{N}_u$  in Fig. 18b and the corresponding increase in  $\tilde{\varepsilon}_n^0$  seen in Fig. 17. For the imposed  $E_{\max} = 1.0$ ,  $\tilde{\varepsilon}_n^0$  reaches a maximum value of 0.8 which is greater than  $\varepsilon_p + \varepsilon_s$  and thus the stress-fiber stresses in the fibers around the  $\phi = 0^\circ$  direction drops significantly and their enthalpy therefore increases resulting in dissociation of stress-fibers around the  $\phi = 0^\circ$  direction. However, the strain values  $\tilde{\varepsilon}_n(\phi \approx \pm 45^\circ)$  are smaller than  $\varepsilon_p + \varepsilon_s$  and thus the stress-fiber stress around  $\phi \approx \pm 45^\circ$  is not significantly reduced similar to the fibers around the  $\phi = 90^\circ$  direction. However, the stress-fibers around the  $\phi \approx \pm 45^\circ$  direction are longer compared to the stress-fibers around the  $\phi = 90^\circ$  direction. This implies that  $\hat{n}(\mu_T - \mu_b)$  of the stress-fibers around the  $\phi \approx \pm 45^\circ$  direction is higher compared to their counterparts around the  $\phi = 90^\circ$  direction and thus these fibers have a lower dissociation rate. It is this combination of effects that results in the stress-fibers around the  $\phi \approx \pm 45^\circ$  direction having the lowest dissociation rate resulting in the butterfly-shaped  $\xi$  distribution.

The results presented in Section 5.1 and 5.2 demonstrate that the model developed here is capable of capturing the full range of reported observations. In particular, the model predicts that sensitivity of the response of cells to the shape of the imposed strain waveform will occur for cells with a fast stress-fiber remodeling rate (undifferentiated cells). By contrast, the strain sensitivity of cells at low imposed cyclic frequencies is predicted to occur in cells with a slow stress-fiber remodeling rate (differentiated cells). The model prediction that cells that display strain sensitivity will not display waveform sensitivity and vice-versa requires experimental validation.

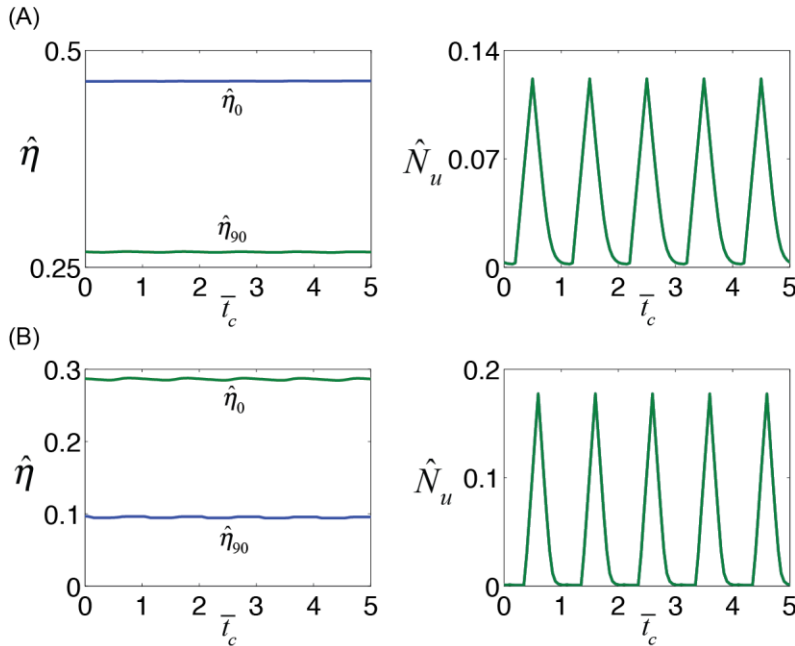


Figure 18: Predictions of the temporal variation of  $\hat{\eta}_0$ ,  $\hat{\eta}_{90}$  and  $\hat{N}_u$  over 5 cycles corresponding to the results in Fig. 17 for cells on substrates (type I experiments) subjected to cyclic loading with (a)  $E_{\max} = 0.4$  and (b)  $E_{\max} = 1.0$ . Cyclic loading is via a symmetric triangular wave with the magnitude of the applied strain-rate fixed at  $|\dot{E}_{11}| = 0.02 \text{ s}^{-1}$ .

## 6. Comparison with existing models

The model presented here falls in a class of continuum models for stress-fiber remodeling initiated by Deshpande et al. (2006) and then extended and modified by Vernerey and Farsad (2011) and more recently Obbink-Huizer et al. (2014). It is instructive to compare and contrast both the formulations and the predictions of these models. The model of Obbink-Huizer et al. (2014) combines the models of Deshpande et al. (2006) and Vernerey and Farsad (2011) and in many ways supersedes these models. We thus restrict the comparison of the current model with that of Obbink-Huizer et al. (2014).

The critical difference between the Obbink-Huizer et al. (2014) model and that presented here is that here we have attempted to motivate the model from thermodynamical considerations while Obbink-Huizer et al. (2014) follow a phenomenological approach. The two key differences that emerge from these different approaches are:

- (i) Obbink-Huizer et al. (2014) model the stress-fiber as a single entity and do not consider the functional units that constitute the stress-fiber. Thus, they inherently assume that the macroscopic imposed strain is equal to the strain within the stress-fiber.
- (ii) The stress dependence in the stress-fiber kinetics is introduced in the formation rate constant in the Obbink-Huizer et al. (2014) model. However, as shown here, thermodynamic considerations dictate that the stress dependence originates from the enthalpy lost in creating stress-fibers. Hence it is the dissociation rate constant in the stress-fiber kinetics that is stress dependent.

The main consequences of these two key differences in the formulation on the predictions are summarized as follows. First, the Obbink-Huizer et al. (2014) cannot predict the dependence of the response of cells on substrates to the shape of the imposed cyclic waveform. The key in understanding the sensitivity of cells to the shape of the waveform is the recognition that the strain-rates within the stress-fibers need not be equal to the macroscopic strain-rates that the cell is subjected to. Second, the Obbink-Huizer et al. (2014) model predict that stress-fibers align with the direction of loading in the type II experiments because the stress-fibers contract perpendicular to the loading direction and thus have a reduced stress level due to the strain dependence of the stress-fiber stress. However, even in differentiated cells with a slow remodeling rate the stress-fibers will remodel over the time-scale of typical experiments and the isometric value of the stress-fiber stress in all directions will be approximately equal. The physics invoked by the Obbink-Huizer et al. (2014) model to explain the observations in the type II experiments is thus questionable. On the other hand, in the current model the stress-fibers align with the imposed loading because contraction in the perpendicular direction implies that those stress-fibers are shorter and comprise fewer functional units. Thermodynamics dictates that these stress-fibers with fewer functional units are less stable and hence stress-fibers form preferentially in the loading direction.

In spite of these differences, the Obbink-Huizer et al. (2014) and current model give qualitatively similar predictions in the limit of slow remodeling. In this limit, the stress-fiber strain is approximately equal to the strain imposed on the cell as assumed a-priori by Obbink-Huizer et al. (2014). However, as discussed above even in this limit the physical basis for the predictions are different. For example Obbink-Huizer et al. (2014) predicting that at cyclic steady-state the stress-fiber stress perpendicular to the loading direction in the type II experiments is approximately zero while the current model will predict that the stress-fiber stress is equal to its initial isometric value of  $\sigma_{\max}$ .

## 7. Concluding remarks

A model for stress-fiber dynamics that includes both the kinetics of stress-fiber formation and dissociation as well as the kinetics of stress-fiber remodeling is presented. The stress-fiber kinetics is motivated by considering the energy-states of the bound and unbound stress-fiber proteins while the remodeling of the stress-fibers is driven by the balance between the loss of internal energy of the stress-fibers and the dissipation resulting from remodeling. These two processes naturally establish the stress, strain and strain-rate dependence of the stress-fiber dynamics. The model is presented in a general three-dimensional framework and includes the transport of the unbound stress-fiber proteins.

Predictions of the model are presented for a wide range of cyclic loadings. First, the model is shown to accurately capture the apparently contrasting observations for cells subjected to cyclic straining on substrates and constrained within a three-dimensional (3D) tissue. Specifically, stress-fibers align perpendicular to the straining directions for cells on 2D substrates while the stress-fibers align along the straining direction for cells constrained in a 3D tissue. These contrasting observations are rationalized by noting that the cell can contract in the direction perpendicular to the loading in the case when it is constrained in a 3D tissue but is constrained against contraction on the 2D substrate. The model predicts that differences in enthalpies develop between the stress-fibers in the different directions due to these different boundary conditions that results in the apparently contrasting observations.

Second, the model was shown to accurately predict a range of observations for the strain, frequency and waveform dependence of the response of cells on 2D substrates subjected to cyclic loading. In line with experimental observations, cells with a fast stress-fiber remodeling rate (representative of undifferentiated cells) are predicted to be sensitive to the imposed lengthening rate while cells with a slow stress-fiber remodeling rate (representative of differentiated cells) are not sensitive to shape of the waveform. By contrast, consistent with other experimental observations, the model predicts that stress-fibers in differentiated cells align perpendicular to the loading direction for imposed strain amplitudes above a critical value even at relatively low values of the imposed strain-rate. Undifferentiated cells with a fast stress-fiber remodeling rate are predicted to not display this sensitivity.

In summary this thermodynamically motivated model rationalizes a wide range of observations for cells subjected to cyclic loading and predicts some key differences between the anticipated responses of differentiated and undifferentiated cells. These predictions require future experimental validation.

### **Appendix A: Chemical potentials of the stress-fiber proteins**

Here we derive expressions for the chemical potential  $\chi_u$  of the aggregate of unbound molecules that form a single functional unit and the chemical potential  $\chi_b$  of a functional unit within a stress-fiber comprising  $n$  units. These chemical potentials are derived using the enthalpies and the constraints imposed on the formation of stress-fibers in deriving the kinetic Eq. (2.16). We shall employ classical statistical mechanics using the assumption of non-interacting particles, i.e. an ideal system.

Consider a segment subtending a unit solid angle within the RVE. Within this segment there are  $\eta$  stress-fibers each comprising  $n$  functional units and aggregates of unbound molecules that form  $N_u/(2\pi)$  functional units. For notational simplicity we denote  $\bar{N}_u \equiv N_u/(2\pi)$ ,  $\bar{N}_b \equiv \eta n$  and  $\bar{N}_T \equiv \bar{N}_u + \bar{N}_b$ . First consider the mixing between the  $\bar{N}_L$  lattice sites and the

$\bar{N}_u$  unbound aggregates of molecules. The  $\bar{N}_u$  identical aggregates of molecules and the  $(\bar{N}_L - \bar{N}_u)$  identical empty lattice sites in the mixture can be arranged in

$$W = \frac{\bar{N}_L!}{\bar{N}_u! (\bar{N}_L - \bar{N}_u)!}, \quad (\text{A1})$$

ways and Boltzmann's entropy formula then gives the entropy of mixing as

$$\Delta S_u = k_B \ln W. \quad (\text{A2})$$

Using Stirling's approximation ( $\ln M! \approx M \ln M - M$  for large  $M$ ) we have

$$\Delta S_u = -k_B [\bar{N}_u \ln \bar{N}_u + (\bar{N}_L - \bar{N}_u) \ln (\bar{N}_L - \bar{N}_u) - \bar{N}_L \ln \bar{N}_L]. \quad (\text{A3})$$

Upon assuming that the entropy of the unbound molecules prior to mixing with the lattice is zero, the chemical potential of the unbound molecules is given by

$$\chi_u \equiv \frac{\mu_u}{n^R} - T \frac{\partial \Delta S_u}{\partial \bar{N}_u} = \frac{\mu_u}{n^R} + k_B T \ln \left[ \frac{\hat{N}_u}{2\pi \hat{N}_L \left(1 - \frac{\bar{N}_u}{\bar{N}_L}\right)} \right], \quad (\text{A4})$$

where  $\hat{N}_L \equiv \bar{N}_L / N_0$ . Since  $\bar{N}_u \ll \bar{N}_L$  (i.e. dilute assumption),  $\chi_u$  simplifies to

$$\chi_u = \frac{\mu_u}{n^R} + k_B T \ln \left( \frac{\hat{N}_u}{2\pi \hat{N}_L} \right). \quad (\text{A5})$$

Now consider the stress-fibers. In deriving the kinetic Eq. (2.16) we have assumed that there exists an intermediate stage where the unbound molecules first cluster into packets comprising unbound molecules that can form  $n$  functional units and some of these packets react to form stress-fibers also comprising  $n$  functional units. To calculate the chemical potentials of the bound molecules within stress-fibers and the unbound molecules in the intermediate stage consider the following two mixing processes. First consider the mixing between  $\bar{N}_u/n$  identical packets of unbound proteins and  $\bar{N}_b/n$  identical packets bound proteins where  $\bar{N}_T \equiv \bar{N}_u + \bar{N}_b$ . Using Boltzmann's entropy formula, the entropy of mixing in this process is

$$\Delta S_b = k_B \ln \left[ \frac{(\bar{N}_b/n + \bar{N}_u/n)!}{(\bar{N}_b/n)! (\bar{N}_u/n)!} \right], \quad (\text{A6})$$

which simplifies using Stirling's approximation to

$$\Delta S_b = -k_B \left[ \left( \frac{\bar{N}_b}{n} \right) \ln \left( \frac{\bar{N}_b}{n} \right) + \left( \frac{\bar{N}_u}{n} \right) \ln \left( \frac{\bar{N}_u}{n} \right) - \left( \frac{\bar{N}_T}{n} \right) \ln \left( \frac{\bar{N}_T}{n} \right) \right]. \quad (\text{A7})$$

The chemical potentials of the bound proteins and unbound proteins after this first step are

$$\chi_{b1} \equiv \frac{\mu_b}{n^R} - T \frac{\partial \Delta S_b}{\partial \bar{N}_b} = \frac{\mu_b}{n^R} + k_B T \ln \left( \frac{2\pi\hat{\eta}\hat{n}}{\hat{N}_u} \right)^{\frac{1}{n}} \quad (\text{A8})$$

and

$$\chi_{I1} \equiv \frac{\mu_u}{n^R} - T \frac{\partial \Delta S_b}{\partial \bar{N}_u} = \frac{\mu_u}{n^R} + k_B T \ln \left( \frac{\hat{N}_u}{2\pi\hat{\eta}\hat{n}} \right)^{\frac{1}{n}}, \quad (\text{A9})$$

respectively, where  $\partial \bar{N}_u / \partial \bar{N}_b = -1$  as the mixing process occurs at constant  $\bar{N}_T$ . Second, recall that the unbound aggregate of proteins occupy lattice sites and thus we mix the  $\bar{N}_u$  unbound protein aggregates with the  $\bar{N}_L$  lattice sites lattice while *not* mixing the  $\bar{N}_u/n$  and  $\bar{N}_b/n$  packets. The entropy of mixing of this process is given by Eqs. (A1) and (A2). Again using the dilute assumption ( $\bar{N}_u \ll \bar{N}_L$ ), the chemical potentials of the bound and unbound molecules in their intermediate stage follow as

$$\chi_b \equiv \chi_{b1} - T \frac{\partial \Delta S_u}{\partial \bar{N}_b} = \frac{\mu_b}{n^R} + k_B T \ln \left[ \left( \frac{2\pi\hat{\eta}\hat{n}}{\hat{N}_u} \right)^{\frac{1}{n}} \left( \frac{\hat{N}_u}{2\pi\hat{N}_L} \right) \right], \quad (\text{A10})$$

and

$$\chi_I \equiv \chi_{I1} - T \frac{\partial \Delta S_u}{\partial \bar{N}_u} = \frac{\mu_u}{n^R} + k_B T \ln \left[ \left( \frac{\hat{N}_u}{2\pi\hat{\eta}\hat{n}} \right)^{\frac{1}{n}} \left( \frac{\hat{N}_u}{2\pi\hat{N}_L} \right) \right], \quad (\text{A11})$$

respectively. In deriving Eqs. (A10) and (A11) we have used the fact that now  $\partial \bar{N}_u / \partial \bar{N}_b = 1$  as in this step we do not change the number of bound and unbound molecules with respect to each but rather calculate the variation in the entropy while changing the number of stress-fiber protein molecules with respect to the fixed number of lattice sites.

Comparing the chemical potentials  $\chi_I$  and  $\chi_u$  we see that the clustering reaction is endergonic and the un-clustering reaction is exergonic when  $\hat{N}_u / (2\pi\hat{\eta}\hat{n}) > 1$  and vice-versa when  $\hat{N}_u / (2\pi\hat{\eta}\hat{n}) < 1$ . This is rationalized by the fact that when the stress-fiber concentration is small compared to the unbound protein concentration, the geometrical constraints imposed by the stress-fibers are small and clustering requires an entropy reduction but the situation is reversed at high stress-fiber concentrations. We emphasize that the unbound proteins in their intermediate clustered state are unstable (due to their low entropy compared to their un-clustered counterparts) and not physically present in the system at any given time. Rather this intermediate state is a transient state in the reaction for the formation/dissociation of the stress-fibers.

Equilibrium between the bound and unbound proteins occurs when their chemical potentials equalize, i.e.  $\chi_u = \chi_b$ . Setting  $\hat{\eta} = 0$  in Eq. (2.16) and simplifying reduces Eq. (2.16) to the condition  $\chi_u = \chi_b$  consistent with the chemical potentials derived here from statistical mechanics considerations.

Finally we note that the free-energy of the stress-fiber proteins within a RVE is given as

$$g = N_u \chi_u + \int_{-\pi/2}^{\pi/2} \int_0^\pi (\eta n \chi_b) \sin \theta d\theta d\varphi, \quad (\text{A12})$$

and this expression can be integrated over the entire cell volume  $V_0$  to give the free-energy of the stress-fiber proteins in the cell as

$$G = \frac{1}{\frac{4\pi}{3} (n^R \ell_0 / 2)^3} \int_{V_0} g \, dV. \quad (\text{A13})$$

### Acknowledgements

AV and VSD acknowledge the Royal Society for supporting AV through a Newton International Fellowship. Insightful discussions with Prof. R.M. McMeeking (UCSB) are gratefully acknowledged.

### References

Aref A, Horvath R, Ramsden JJ (2010), Spreading kinetics for quantifying cell state during stem cell differentiation. *Journal of Biological Physics and Chemistry*, 10, 145-151.

Buck RC (1980), Reorientation response of cells to repeated stretch and recoil of the substratum. *Experimental Cell Research*, 127(2), 470-474.

Burridge K, Chrzanowska-Wodnicka M (1996), Focal adhesions, contractility and signaling. *Annual Review of Cell and Development Biology*, 12, 463-469.

Byers HR, Fujiwara K (1982), Stress-fibers in cells in situ: immunofluorescence visualization with antiactin, antimyosin and anti-alpha-actinin. *Journal of Cell Biology*, 93, 804-811.

Chen CS, Alonso JL, Ostuni E, Whitesides GM, Ingber DE (2003), Cell shape provides global control of focal adhesion assembly. *Biochemical and Biophysical Research Communications*, 307: 355-361.

De Bruyn PPH, Cho Y (1974), Contractile structures in endothelial cells of splenic sinusoids. *Journal of Ultrastructure Research*, 49, 24-33.

Deshpande VS, McMeeking RM, Evans AG (2006), A bio-chemo-mechanical model for cell contractility. *Proceedings of the National Academy of Sciences USA*, 103, 14015-14020.

Discher DE, Janmey P, Wang YL (2005), Tissue cells feel and respond to the stiffness of their substrate. *Science*, 310, 1139-1143.

Eisenberg E, Hill TL, Chen Yi-Der (1980), Cross-bridge model for muscle contraction. *Biophysical Journal*, 29, 195-227.

Evans E, Ritchie K (1997), Dynamic strength of molecular adhesion bonds. *Biophysical Journal*, 72, 1541-1555.

Faust U, Hampe N, Rubner W, Kirchgessner N, Safran S, Hoffmann B, Merkel R (2011), Cyclic stress at mHz frequencies aligns fibroblasts in direction of zero strain. *PLoS One* 6(12):e28963.

Foolen J, Deshpande VS, Kanters FMW, Baaijens FPT (2012), The influence of matrix integrity on

stress-fiber remodeling in 3D. *Biomaterials*, 33, 7508-7518.

Gauvin R, Parenteau-Bareil R, Larouche D, Marcoux H, Bisson F, Bonnet A, Auger FA, Bolduc S, Germain L (2011), Dynamic mechanical stimulations induce anisotropy and improve the tensile properties of engineered tissues produced without exogenous scaffolding. *Acta Biomaterialia*, 7(9), 3294-3301.

Gordon SR, Essner E, Rothstein H (1982), In situ demonstration of actin in normal and injured ocular tissues using 7-nitrobenz-2-oxa-1,3-diazole phalloidin. *Cell motility and the cytoskeleton*, 4, 343-354.

Guterl KA, Haggart CR, Janssen PM, Holmes JW (2007), Isometric contraction induces rapid myocyte remodeling in rat right ventricular papillary muscles. *American Journal of Heart and Circulatory Physiology*, 293, H3706-H3712.

Hill AV (1938), The heat of shortening and the dynamic constants of muscle. *Proceedings of the Royal Society B*, 126, 136-195.

**Howard J. (2001), *Mechanics of motor proteins and the cytoskeleton*. Sinauer Associated Inc.**

Hunter P (1995), Myocardial constitutive laws for continuum mechanics models of the heart. In *Molecular and Subcellular Cardiology*, Eds. S. Sideman, R. Beyar, 303-318. Springer.

Jungbauer S, Gao H, Spatz JP, Kemkemer R (2008), Two characteristic regimes in frequency-dependent dynamic reorientation of fibroblasts on cyclically stretched substrates. *Biophysical Journal*, 95(7):3470–3478.

Kaunas R, Nguyen P, Usami S, Chien S (2005), Cooperative effects of Rho and mechanical stretch on stress-fiber organization. *Proceedings of the National Academy of Sciences USA*, 102(44), 15895-15900.

Kolega J (1986), Effects of mechanical tension on protrusive activity and microfilament and intermediate filament organization in an epidermal epithelium moving in culture. *Journal of Cell Biology*, 102, 1400-1411.

Langanger G, Moeremans M, Daneels G, Sobieszek A, De Brabander M, De Mey J (1986), The molecular organisation of myosin in stress-fiber of cultured cells. *Journal of Cell Biology*, 102, 200-209.

Lucas SM, Ruff RL, Binder MD (1995), Specific tension measurements in single soleus and medial gastrocnemius muscle fibers of the cat. *Experimental Neurology*, 95, 142-154.

McGarry JP, Fu J, Yang MT, Chen CS, McMeeking RM, Evans AG, Deshpande VS (2009), Simulation of the contractile response of cells on an array of micro-posts. *Philosophical Transactions of the Royal Society A*, 367(1902), 3477-3497.

McGrath JL, Tardy Y, Dewey CF, Meister JJ, Hartwig JH (1998), Simultaneous measurements of actin filament turnover, filament fraction and monomer diffusion in endothelial cells. *Biophysical Journal*, 75, 2070-2078.

McMahon TA (1984), *Muscles, Reflexes and Locomotion*, Princeton University Press, New Jersey.

Mochitate K, Pawelek P, Grinnell F (1991), Stress relaxation of contracted collagen gels: disruption of actin filament bundles, release of cell surface fibronectin, and down-regulation of DNA and protein synthesis. *Experimental Cell Research*, 193, 198-207.

- Neidlinger-Wilke C, Grood ES, Wang JH-C, Brand RA, Claes L (2001), Cell alignment is induced by cyclic changes in cell length: studies of cells grown in cyclically stretched substrates. *Journal of Orthopedic Research*, 19(2), 286-293.
- Nieponice A, Maul TM, Cumer JM, Soletti L, Vorp DA (2007), Mechanical stimulation induces morphological and phenotypic changes in bone marrow-derived progenitor cells within a three-dimensional fibrin matrix. *Journal of Biomedical Materials Research A*, 81(3), 523-530.
- Obbink-Huizer C, Oomens CWJ, Loerakker S, Foolen J, Bouten CVC, Baaijens FPT (2014), Computational model predicts cell orientation in response to a range of mechanical stimuli, *Biomechanics and Modeling in Mechanobiology*, 13, 227-236.
- Parker KK, Brock AL, Brangwynne C, Mannix RJ, Wang N, Ostuni E, Geisse NA, Adams JC, Whitesides GM, Ingber DE (2002), Directional control of lamellipodia extension by constraining cell shape and orienting cell tractional forces. *FASEB Journal*, 16, 1195-1204.
- Pathak A, McMeeking RM, Evans AG, Deshpande VS (2011), An analysis of the co-operative mechano-sensitive feedback between intracellular signaling, focal adhesion developed and stress-fiber contractility. *ASME Journal of Applied Mechanics*, 78, 041001-1.
- Ronan W, Deshpande VS, McMeeking RM, McGarry JP (2012), Numerical investigation of the active role of the actin cytoskeleton in the compression resistance of cells. *Journal of the Mechanical Behavior of Biomedical Materials*, 14, 143-157.
- Tan JL, Tien J, Pirone DM, Gray DS, Bhadriraju K, Chen CS (2003), Cells lying on a bed of microneedles: an approach to isolate mechanical force. *Proceedings of the National Academy of Sciences USA*, 100, 1484-1489.
- Thavandiran N, Dubois N, Mikryukov A, Massé S, Beca B, Simmons CB, Deshpande VS, McGarry JP, Chen CS, Nanthakumar K, Keller K, Radisic M, Zandstra PW (2013), Design criteria-guided formulation of pluripotent stem cell-derived cardiac microtissues. *Proceedings of the National Academy of Sciences, USA*, 110, E4698-E4707.
- Thomopoulos S, Fomovsky GM, Holmes JW (2005), The development of structural and mechanical anisotropy in fibroblast populated collagen gels. *Journal of Biomechanical Engineering ASME*, 127, 742-750.
- Tondon A, Hui-Ju H, Kaunas R (2012), Dependence of cyclic stretch-induced stress-fiber reorientation on stretch waveform. *Journal of Biomechanics*, 45, 728-735.
- Vernerey FJ, Farsad M (2011), A constrained mixture approach to mechano-sensing and force generation in contractile cells. *Journal of the Mechanical Behavior of Biomedical Materials*, 4(8), 1683-1699.
- Vigliotti A, McMeeking RM, Deshpande VS (2015), Simulation of the cytoskeletal response of cells on grooved or patterned substrates. *Journal of the Royal Society Interface*, 12, 20141320.
- Wang JH, Thampatty BP (2006), An introductory review of cell mechanobiology. *Biomechanics and Modeling in Mechanobiology*, 5, 1-16.
- Wei Z, Deshpande VS, McMeeking RM, Evans AG (2008), Analysis and interpretation of stress-fiber organization in cells subject to cyclic stretch. *Journal of Biomechanical Engineering ASME*, 130, 031009-1.